Monthly Notices of the ROYAL ASTRONOMICAL SOCIETY

MNRAS **532,** 4661–4680 (2024) https://doi.org/10.1093/mnras/stae1633
Advance Access publication 2024 July 4

Herschel Gould Belt Survey in Taurus – II. A census of dense cores and filaments in the TMC1 region

J. M. Kirk [1]★ D. Ward-Thompson [1] J. Di Francesco,[2] Ph. André,[3] D. W. Bresnahan,[1] V. Könyves [1] K. Marsh [4,5] M. J. Griffin,[4] N. Schneider [6] A. Men'shchikov,[3] P. Palmeirim [7] S. Bontemps [8] D. Arzoumanian [9] M. Benedettini [10] and S. Pezzuto [10]

[1]*Jeremiah Horrocks Institute, University of Central Lancashire, Preston, Lancashire, PR1 2HE, UK*
[2]*National Research Council of Canada, Herzberg, Astronomy & Astrophysics Research Centre, 5071 West Saanich Road, Victoria (BC), V9E 2E7, Canada*
[3]*Laboratoire Astrophysique (AIM), Université Paris-Saclay, Université Paris Cité, CEA, CNRS, AIM, F-91191 Gif-sur-Yvette, France*
[4]*School of Physics and Astronomy, Cardiff University, Queens Buildings, The Parade, Cardiff, Wales CF24 3AA, UK*
[5]*IPAC, Caltech, 1200E California Boulevard, Pasadena, CA 91125, USA*
[6]*Physikalisches Institut, Universität zu Köln, Zülpicher Str. 77, D-50937 Köln, Germany*
[7]*Instituto de Astrofísica e Ciências do Espaço, Universidade do Porto, CAUP, Rua das Estrelas, P-4150-762 Porto, Portugal*
[8]*Laboratoire d'astrophysique de Bordeaux, Univ. Bordeaux, CNRS, B18N, allée Geoffroy Saint-Hilaire, F-33615 Pessac, France*
[9]*National Astronomical Observatory of Japan, 2-21-1 Osawa, Mitaka, 181-8588 Tokyo, Japan*
[10]*INAF – Istituto di Astrofisica e Planetologia Spaziali, via Fosso del Cavaliere 100, I-00133 Roma, Italy*

Accepted 2024 June 26. Received 2024 June 24; in original form 2023 September 26

ABSTRACT

We present a catalogue of dense cores and filaments in a 3.8° × 2.4° field around the TMC1 region of the Taurus molecular cloud. The catalogue was created using photometric data from the *Herschel* SPIRE and PACS instruments in the 70, 160, 250, 350, and 500 μm continuum bands. Extended structure in the region was reconstructed from a *Herschel* column density map. Power spectra and probability density functions (PDFs) of this structure are presented. The PDF splits into lognormal and power-law forms, with the high-density power-law component associated primarily with the central part of TMC1. The total mass in the mapped region is 2000 $M_\odot$, of which 34 per cent is above an extinction of $A_V \sim 3$ mag – a level that appears as a break in the PDF and as the minimum column density at which dense cores are found. A total of 35 dense filaments were extracted from the column density map. These have a typical full width at half-maximum (FWHM) width of 0.07 pc, but the TMC1 filament itself has a mean FWHM of ∼ 0.13 pc. The thermally supercritical filaments in the region are aligned orthogonal to the prevailing magnetic field direction. Derived properties for the supercritical TMC1 filament support the scenario of it being relatively young. A catalogue of 44 robust and candidate prestellar cores is created and is assessed to be complete down to 0.1 $M_\odot$. The combined prestellar core mass function for the TMC1 and L1495 regions is well fit by a single lognormal distribution and is comparable to the standard initial mass function.

Key words: catalogues – stars: formation – ISM: clouds – ISM: individual objects: TMC1 molecular cloud – ISM structure – submillimetre: ISM.

1 INTRODUCTION

Stars form within the dense cores of giant molecular clouds. Observations with the *Herschel* Space Observatory (Pilbratt et al. 2010) have reinforced the paradigm that these cores form preferentially as condensations on filaments within the clouds (e.g. André et al. 2014). The success of *Herschel* in this regard is due to its unparalleled ability to map simultaneously in five submillimetre wavelengths large contiguous areas of sky with unprecedented dynamic range and sensitivity. The *Herschel* Gould Belt Survey (HGBS; André et al. 2010) has used this ability to map systematically star formation regions in the Gould Belt (a ∼ 1 kpc loop of molecular clouds that encircle the local bubble; see Herschel 1847; Gould 1879). Catalogues and analysis of dense cores in Aquila (Könyves et al. 2015), Corona Australis (Bresnahan et al. 2018), and Lupus (Benedettini et al. 2018) have already been published.

Taurus forms broadly two large parallel structures which have been mapped with *Herschel* (Kirk et al. 2013). The overall mapping approach is described in Kirk et al. (2013). The first part of the Taurus catalogue was published in Marsh et al. (2016, hereafter Paper I). Paper I found a total of 52 prestellar cores out of a large population of 525 unbound starless cores across an area of ∼ 4° × 2°. They showed that the completeness-corrected mass function for the unbound starless cores was consistent with a power-law form below a mass of 0.3 $M_\odot$. This correspondence was unlike the mass function for bound prestellar cores which followed the classical lognormal form, in agreement with previous studies.

★ E-mail: jmkirk@uclan.ac.uk

Table 1. Filter-dependent observation details.

Filter	λ [μm]	σ_{cal} [%]	HPBW [']	S_{Planck} [MJy sr^{-1}]
PACS blue	70	10	8.4	4.62
PACS red	160	10	14	77.4
SPIRE PSW	250	12	18.2	59.4
SPIRE PMW	350	12	25	36.9
SPIRE PLW	500	12	36	17.1

Note. Columns 1 and 2 list the filter name and wavelength. Column 2 lists the assumed calibration uncertainty. Column 4 lists the effective HPBW of the telescope at this wavelength. Column 5 lists the median *Planck* intensity level across the map (see Section 4).

The area mapped in Paper I was the L1495 region. Its dominant feature is the B211/213 filament which stretches across $\sim$ 2 degrees ($\sim$ 5 pc at 140 pc). Palmeirim et al. (2013) showed that the B211/213 was an archetypical case of material being funnelled along low-density striations onto the central filament. For example, the striations and filament were respectively oriented parallel and perpendicular to the local magnetic field direction. The next HGBS tile across from the L1495 region, along the northern structure, is the one presented in this paper. It is markedly different from the B211/213 and L1495 region as it lacks any dominant singular filament and is instead composed of a network of distributed filaments and structures (see Fig. 2 and Section 4). For ease of reference, we refer to this entire region, i.e. the area mapped in this paper, as the 'TMC1 region'.

This paper is laid out as follows. Section 2 describes the *Herschel* observations of the TMC1 region and the data reduction process. Section 3 characterizes the distance to the TMC1 region. Section 4 describes the creation of a column density map from the *Herschel* observations and includes an analysis of its power spectrum and hierarchical structure. In Section 5, we characterize the filamentary structure within the TMC1 region and compare it to the bulk magnetic field and the location of the cores in our catalogue. In Section 6 we describe our source extraction methodology, the resulting catalogue of cores, and the catalogue's general properties, and the properties of the prestellar core mass function in Taurus.

2 OBSERVATIONS

The *Herschel* Space Observatory was a 3.5-m diameter passively cooled Cassegrain space telescope launched on the 2009 May 14 (Pilbratt et al. 2010). It operated two photometric instruments in the far-infrared and submillimetre regimes – the Photodetector Array Camera and Spectrometer (PACS; Poglitsch et al. 2010) and the Spectral and Photometric Imaging Receiver, (SPIRE; Griffin et al. 2010; Swinyard et al. 2010) – to provide sufficient wavelength coverage to bracket the peak of the 10 K cold dust spectral energy distribution (SED). Table 1 lists the instrument and filter names, the wavelengths of the filters, and our assumed calibration errors.

The HGBS[1] (André et al. 2010) mapped the Taurus molecular cloud (TMC) using its SPIRE/PACS parallel-scanning mode. The mapping scheme is described in Kirk et al. (2013), this paper presents data from Tile N2 of that scheme. The observation details for this tile are listed in Table 2. The parallel mode observes simultaneously with all three SPIRE filters and two of the three PACS filters, and the scanning speed was 60 arcsec s^{-1}. The tile was observed twice, in perpendicular mapping directions, to aid in the removal of $1/f$ noise. The TMC1 observations used the 70/160 μm PACS filter set. In parallel-mode, the effective PACS half-power beam width (HPBW) at 160 μm was degraded due to the elongation of the point spread function (PSF) in the scan direction caused by sampling limitations imposed by the SPIRE/PACS Parallel Mode. The resulting telescope HPBWs are also listed in Table 1.

The SPIRE data were reduced to level 1 status (flux calibrated timelines) using HIPE version 10 (Ott 2010). The SPIRE thermistor timelines were visually inspected for discontinuities caused by instrumental factors. These were corrected before the timelines were processed. The data were de-glitched using the concurrent and wavelet deglitcher tasks. Residual glitches were identified in restored maps and manually flagged as bad in the timeline data. Flux calibration, temperature drift correction, and bolometer time response corrections were done with the standard SPIRE pipeline tasks using version 10.1 of the SPIRE calibration product. The level 1 timelines for each contiguous region were merged into a single level 1 product. The differences in relative bolometer-to-bolometer gain were corrected using SPIRE calibration product version 10.1. Residual $1/f$ noise in the observation baselines was removed by using the destriper task in HIPE. The final SPIRE maps were made using the naive map maker and were produced on pixel grids of 6, 10, and 14 arcsec pixels for the 250-, 350-, and 500-μm maps, respectively.

The PACS data were reduced to level 1 status using HIPE version 10.0 (build 2843) with the standard PACS pipeline. Bad and saturated pixels were masked during the reduction process, glitches were removed following the procedure described in Könyves et al. (2015), and version PACS_CAL_69_0 of the PACS calibration product was applied. For map making, the level 1 timelines were exported to the IDL SCANAMORPHOS map maker (version 20.0; Roussel 2013) which was used to remove thermal and non-thermal brightness drifts and any residual glitches. The resulting PACS maps were produced on a 3 arcsec per pixel grid.

3 TMC1 DISTANCE

The TMC is one of the nearest star formation regions to the Sun. Tomographic analysis of the GAIA distances and tracers of molecular material has shown that the full TMC is a U-shaped structure that points away from us and the local bubble (Ivanova et al. 2021; Dharmawardena et al. 2022). The depth of the material may be 20 pc or more; the TMC1 region is on the leading edge of that structure (Ivanova et al. 2021).

The traditional distance to the Taurus region is usually taken as 140 pc (Straizys & Meistas 1980; Kenyon, Dobrzycka & Hartmann 1994; Loinard et al. 2008). However, the launch of the GAIA parallax mission has allowed newer studies to probe the distance and three-dimensional structure of the cloud (Luhman 2018; Fleming et al. 2019; Galli et al. 2019).

There is an extended young stellar object (YSO) population across Taurus (e.g. Esplin & Luhman 2019). Distances are attributed to parts of the TMC by grouping GAIA sources into clusters/groups and then associating the mean distance of that cluster to part of the cloud. If a single cluster is associated with the entire region, the mean distance assigned is 141–142 pc (Luhman 2018; Esplin & Luhman 2019; Krolikowski, Kraus & Rizzuto 2021). Splitting those stars into two cluster groups gives distances 138 ± 1.9 and 142 ± 2 (Galli et al. 2019).

These studies use catalogues of YSOs with a range of ages, some of which may be more evolved and thus dissociated from the material from which they formed. We double-check the distance attribution

[1] http://gouldbelt-herschel.cea.fr

Table 2. TMC observation details.

Field	RA	Dec.	AOR	Duration	OD	UT date	Scan dir
N2	$4^h37^m31.1^s$	$+26°01'22''$	1342202252	10086	451	2010-08-07	N
	$4^h37^m31.1^s$	$+26°01'22''$	1342202253	14453	451	2010-08-07	O

Note. Column 1 lists the tile name. Columns 2 and 3 list the RA and Declination (J2000) of the field centre. Column 4 lists the observations' AOR identification number. Column 5 lists the OD, the day of the observation numbered from the launch of the spacecraft, and column 6 lists the UT date of the observation. Column 7 lists the scan direction of the field – N for nominal, O for an orthogonal cross-scan.

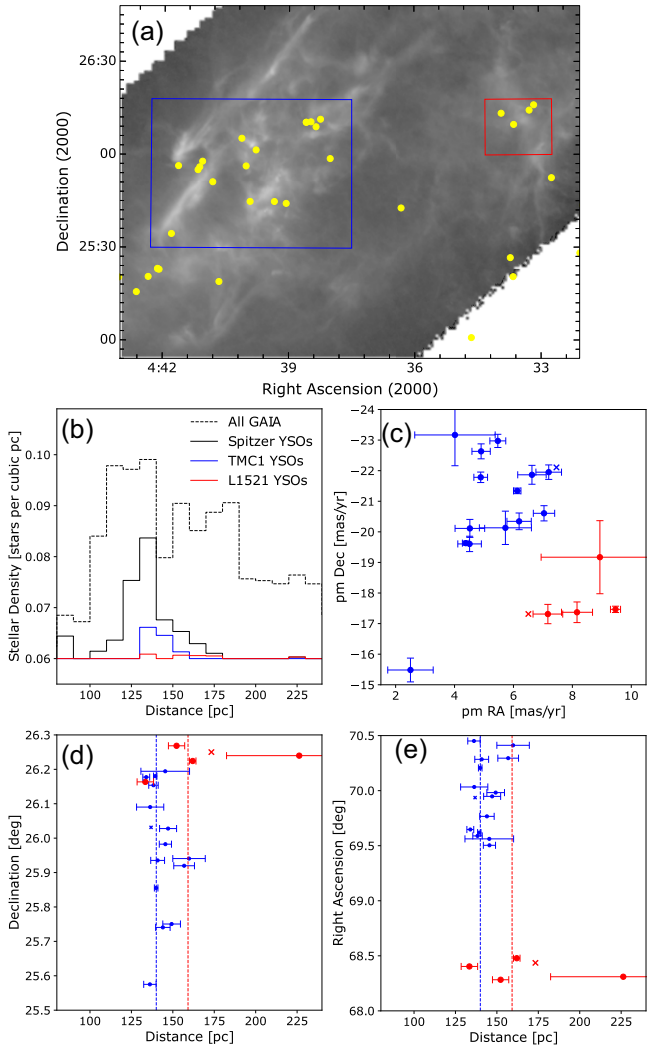

Figure 1. The distribution of *Spitzer* detected YSOs with GAIA DR3 distances towards the TMC1 region. (a) The positions of Spitzer detected YSO candidates (yellow markers; Rebull et al. 2010) with a *GAIA* distance in our field. The grayscale is the $N(H_2)$ column density map as per Fig. 2. The blue box denotes those YSOs associated with TMC1 while the red box shows those associated with L1521. Sources within those boxes are colour-coded blue (TMC1) and red (L1521) in the other plots in this figure. (b) The number volume density of GAIA sources across the field studied in this paper. The solid black line shows all GAIA sources, the dash black line shows all *Spitzer* YSOs, the blue curve show YSOs associated with TMC1, and the red curve shows YSOs associated with L1521. (c), (d), and (e) show the distribution of the TMC1 (blue) and L1521 (red) YSOs in parameter space. The dashed lines show the weighted average distances to TMC1 (blue) of 140.0 ± 0.6 pc and L1521 (red) of 159 ± 2 pc.

by selecting only those GAIA sources with a *Spitzer* detection from Rebull et al. (2010). Infrared-detected sources should be the younger subset of young stars in the region and, thus, those most likely to be still associated with their natal cloud. Fig. 1(a) shows the location of YSOs and YSO candidates reported by Rebull et al. (2010). Two groups of YSOs towards TMC1 and L1521 are indicated. Fig. 1(b) shows that the distance trend for all GAIA sources in this field is to peak at 140 pc and drop away at higher distances, the assumption being that sources behind the Taurus cloud are extincted by it. The YSOs towards this part of Taurus also peak at 140 pc, albeit with a short tail at higher distances. Fig. 1(c) to e show that the TMC1 and L1521 sources are well separated in proper motion. However, the L1521 YSOs appear to occupy a spread of distances with a mean of 159 ± 2 pc. Sources towards TMC1 are more tightly clustered with a mean distance of 140.0 ± 0.6.

Therefore despite different clustering techniques, sample preferences, and methods – the underlying distance for the TMC1 region remains resolutely stuck at its historical value of 140 pc. It is a value that may no longer be as useful for the wider region but has been shown to repeatedly hold as the preferred distance to TMC1/Heiles Cloud 2 (HCL2)/L1521. Therefore, we adopt 140 pc as the distance to structures studied in this paper. The caveat is that 140 pc is the mean distance to the young stellar sources associated with the cloud; their projected scatter (Esplin & Luhman 2019; Galli et al. 2019; Krolikowski et al. 2021) and the width of the cloud (Fig. 1) is on the order of a degree. At 140 pc this equates to a plane-of-the-sky distance of 2.4 pc.

4 EXTENDED STRUCTURE

Figs A1–A5 show the five *Herschel* flux density maps towards the TMC1 region. There is a change in the morphology of the emission with wavelength. The 70-μm map only shows compact thermal emission from young protostars. The 160-μm map shows more extended structure, with the 160- and 250-μm maps showing significant levels of cirrus-like clouds. At 350 and 500 μm, the maps show thick, colder filaments and dense cores begin to stand out. To analyse star formation within the TMC1 region, we need to be able to extract the most appropriate structures from this assemblage. We assume a single isothermal dust temperature along the line of sight. In this section, we use a $N(H_2)$ column density map to examine the extended structures associated with the colder dust, and in the following section, we look at the properties of cores extracted from these five maps.

4.1 Column density maps

An $N(H_2)$ column density map was created on the 250-μm pixel grid and at the 500-μm resolution using the method described in Kirk et al. (2013). In summary, the median intensity level at each

wavelength was bootstrapped to the median intensity estimated from *Planck* & IRAS (cf. Bernard et al. 2010, see Table 1 for the estimated levels) and the data were convolved to the SPIRE 500-μm beam PSF using the convolution kernels of Aniano et al. (2011). The function $F_\nu = M B_\nu(T)\kappa_\nu / D^2$ was then fit to the SED of each pixel from 160 to 500 μm where F_ν is the monochromatic intensity, M is the dust mass, $B_\nu(T)$ is the Planck function at temperature T, and D is the average assumed distance to the TMC1 region (140 pc). The dust mass opacity κ_ν was parameterized as $\kappa_\nu \propto \nu^2$ (i.e. assuming $\beta = 2$) and was referenced against a value of 0.1 $\mathrm{cm^2\,g^{-1}}$ at 300 μm (Hildebrand 1983). In converting dust mas to molecular gas mass we assumed a dust-to-molecular hydrogen mass ratio of 100. The minimisation package MPFIT (Markwardt 2009) was used for the fitting and the per-pixel flux errors included contributions from the map rms, DC level estimation, and calibration uncertainty (for details, see Kirk et al. 2013).

Fig. 2 (top panel) shows the $N(\mathrm{H_2})$ map at 36 arcsec resolution. The field comprises a contiguous region (in the plane of the sky) of high column density material in the north-eastern (left) part of the field. This feature is HCL2 (Heiles 1968). HCL2 was one of the dark clouds where normal OH emission was first detected (Heiles 1968). The hole at approximately 4:40:45, + 25:45:00 has led to the features surrounding it being dubbed the 'Taurus Molecular Ring', albeit one that breaks up into individual dense cores when viewed in more detail (Tóth et al. 2004). The most prominent part of this ring is TMC No. 1 (TMC1), a $\sim 0.5^\circ$ long linear feature on its north-east side. The western feature (right) is the original position of the original L1521 dark nebula (Lynds 1962).

Fig. 2 also shows the temperature map also derived from the modified blackbody SED fitting. Comparing the Molecular Ring column density structure to the dust temperature map (lower panel) shows that the parts with the highest column densities are associated with cold dust. In those parts, the temperatures drops to 11–12 K, down from the general $\sim$ 14 K found over most of the region. The *Herschel* emission is a product of different temperature elements along the line of sight, so the dust temperature produced from it will be a characteristic average.

TMC1 was studied in IRAS and SCUBA dust emission by Nutter et al. (2008) who dubbed it the 'Bull's Tail'. After background subtraction, they found that the filament was consistent with a narrow, cold ($\sim$ 8 K) core and a broader warmer ($\sim$ 12 K) jacket. The Bull's Tail is visible as a cool feature (the red strip in the bottom panel of Fig. 2). Indeed, this filament was sufficiently dense to show in absorption in a *Spitzer* 70-μm map (Nutter et al. 2008). Following Pezzuto et al. (2021), the SED fit used to produce the column density map was used to create an expected map of 70-μm intensity. The expected map showed absorption in places of high-column density, something not seen in the original PACS 70-μm intensity map. Pezzuto et al. (2021) found the same pattern in Perseus and ruled out errors in the fitting of the dust temperature as a cause of the discrepancy of the actual and expected 70-μm intensity. That this extinction is seen with *Spitzer*, but not *Hershel* could imply a methodological cause (i.e. the way the data was processed in either study).

As mentioned previously, the structure visible in Fig. 2 is markedly different than that seen in the neighbouring L1495 region (cf. fig. 3 of Palmeirim et al. 2013 or fig. 1 of Paper I) which is dominated by a single strong trunk filament. By contrast, the TMC1 region is more complex and nest-like, albeit with some fainter but strongly linear features of its own (see Section 5). This is similar to the ridge-nest structures observed in the Vela C region (Hill et al. 2011), albeit on a smaller physical scale.

4.1.1 Comparison with previous maps

We check the absolute calibration of the $N(\mathrm{H_2})$ map by using the *Planck* 353 GHz (850 μm) dust optical-depth map of the region (Planck Collaboration XI 2014). The *Herschel* $N(\mathrm{H_2})$ map was smoothed to the same resolution as the *Planck* map (5′ HPBW). A *Planck* column density map was then extrapolated from their published optical depth and temperature maps using the same reference properties used for the *Herschel* map. Both column density maps were then regridded to a common pixel grid. Fig. 3 (left) shows a pixel-by-pixel comparison of the column densities from the two maps. The horizontal axis shows the *Herschel* $N(\mathrm{H_2})$ column density at 5 arcmin while the vertical axis shows the extrapolated *Planck* column density. The solid red line shows a 1:1 correlation and the two dashed lines show a 10 per cent variance from that in either property.

Fig. 3 (left) shows a small dip away from equivalence below $\sim 1.5 \times 10^{21}$ $\mathrm{cm^{-2}}$. This deviation could be attributed to warmer, low-density material to which *Herschel* is more sensitive than *Planck* (due to its coverage at shorter wavelengths). A linear fit to the data above this point gives an excellent correlation to the data (shown by the green line). The two results show that the offset-correction method from Bernard et al. (2010) has well reproduced the absolute level of emission in the map.

The *Herschel* column densities can be converted into an equivalent visual extinction using standard assumptions (Bohlin, Savage & Drake 1978). The central panel of Fig. 3 shows a comparison between these values and the visual extinction values towards HCL2 calculated from the POSS plates by Cernicharo & Bachiller (1984). The values show good agreement over the range of 1–5 mag. A similar comparison was made to the A_K extinctions calculated from 2MASS sources (Schneider et al. 2011) and is shown in Fig. 3 (right). A regression over the data binned in logarithmic bins shows a linear relation of $A_K \propto A_V^{0.99\pm0.06}$ for the TMC1 region. This equivalence differs from that seen in Orion A where a non-linear relationship was found and interpreted as evidence for grain growth (Roy et al. 2013). Likewise, Uehara et al. (2021) interpreted a larger average dust grain size in Orion A, compared to Taurus, as evidence of grain growth. Therefore, the linearity of the data in this work would be consistent with the reported differences between Taurus and Orion A.

4.1.2 High resolution column density map

A second 'High Resolution' column density map was created following the method described in appendix A of Palmeirim et al. (2013). This method works by combining the unique features from each of three column density maps with 36, 24, and 18 arcsec resolution (equivalent to 500-, 350-, and 250-μm HPBW, respectively). The 36 arcsec map is the same as the map described above. The 24 arcsec map was created using the same technique as the 36 arcsec map, but was made at the 350-μm resolution and did not include the 500-μm data point in the fitting. A colour-temperature map was created from the ratio of the 160-/250-μm data. For an assumed set of dust parameters – same as above – the 160-/250-μm ratio only depends on the dust temperature. The colour temperature estimated from the 160-/250-μm ratio was then used with the 250-μm intensity to calculate a dust mass following the same assumptions as for the regular fitting.

Line-of-sight effects mean that the 'high-resolution column density' method will underestimate the true column density (as will any per-pixel fitting of absolute fluxes) and combining the different resolutions does increase the noise in the final map (Juvela &

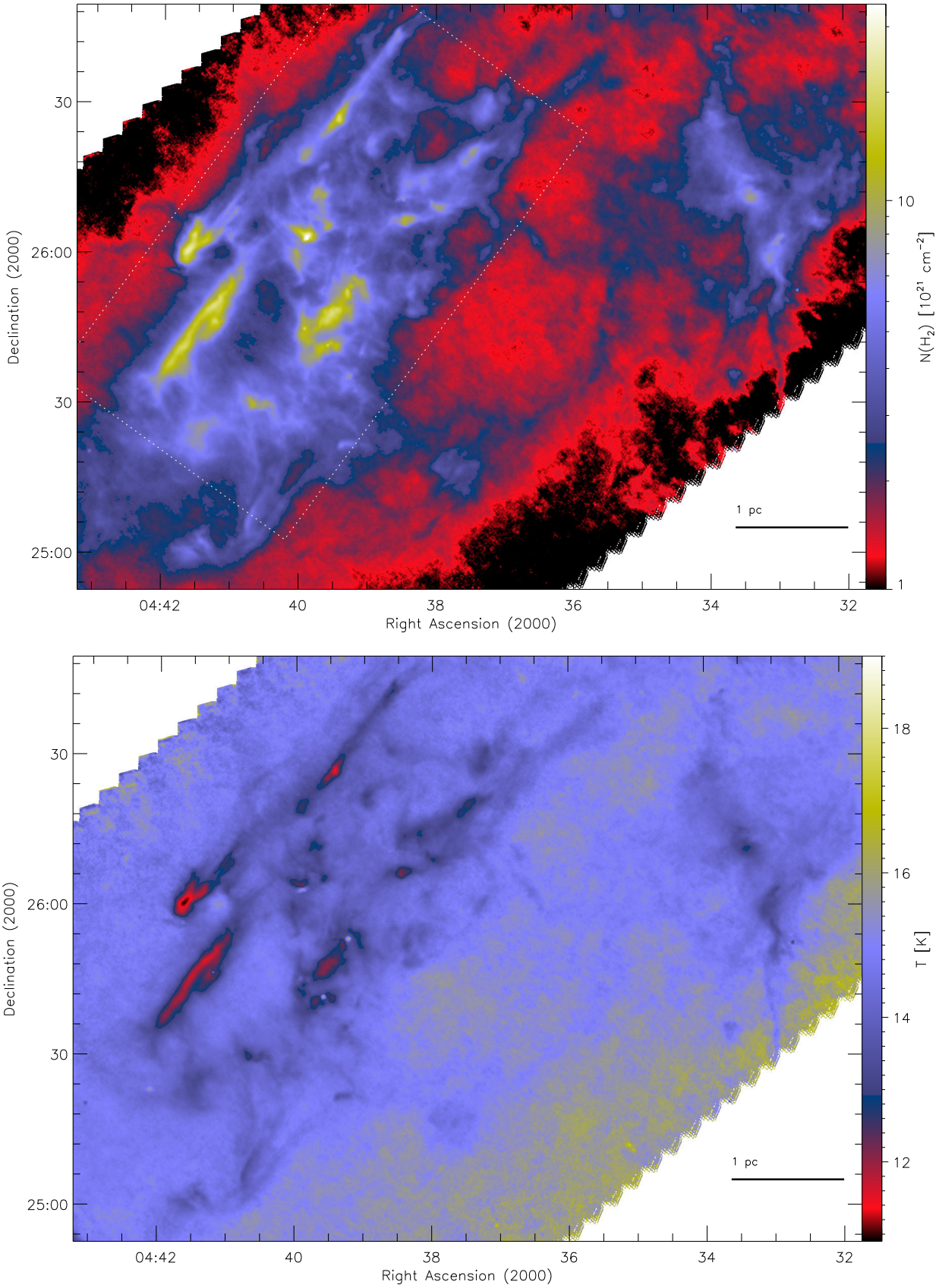

Figure 2. Maps of $N(H_2)$ column density (*top*) and dust temperature (*bottom*) towards the TMC1 region derived from *Herschel* 160- to 500-μm data. The colour bars show the range of the displayed quantities. The effective resolution of the maps is 36 arcsec. The horizontal yardstick shows 1 pc at the assumed distance to Taurus (140 pc). The dotted box in the upper figure shows the region used to determine the probability density functions in Section 4.4 and Fig. 6.

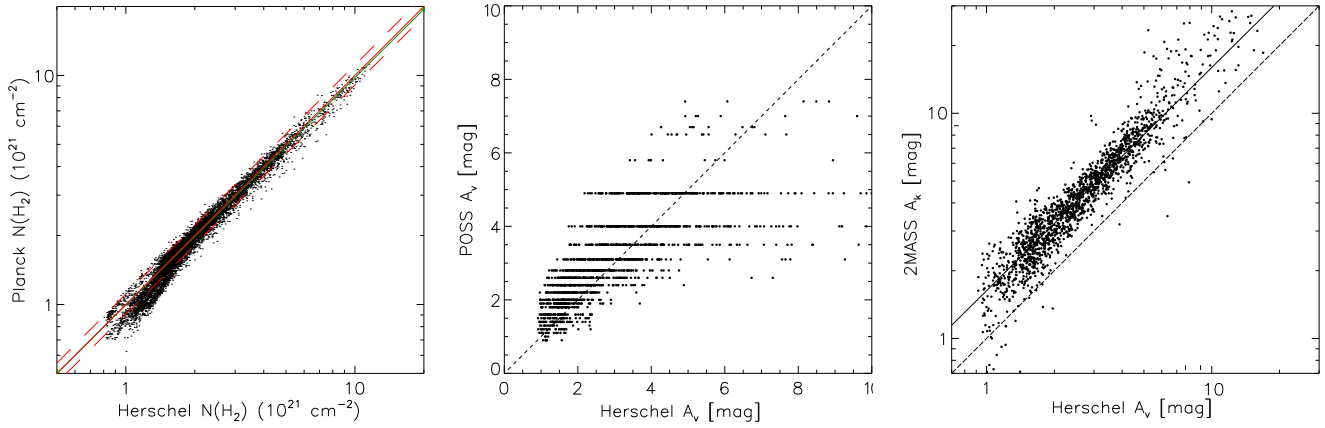

Figure 3. Point-by-point comparisons of the *Herschel* column density values (or equivalent visual extinctions) and equivalent data sets. *(Left)* A position-by-position comparison of the *Herschel* column densities smoothed to a 5 arcmin HPBW versus an equivalent column density calculated from the *Planck* 353 GHz optical depth. The two dashed red lines show a deviation of 10 per cent away from a strict 1:1 relationship (the solid red line). A best-fitting power-law relation (fitted above 1.5×10^{21} cm^{-2}) between the two is shown by a green line and has the form $N(\mathrm{H_2})_{\mathrm{Planck}} = 0.994 \pm 0.002 \times N(\mathrm{H_2})_{\mathrm{Herschel}}^{0.993 \pm 0.002}$. *(Centre)* A comparison of A_V calculated from the *Herschel* column densities versus the A_V estimated from the POSS plates towards HCL2 (Cernicharo & Bachiller 1984). The dashed line is a line of equivalence. *(Right)* A comparison of A_V calculated from the *Herschel* column densities versus the K-band extinction calculated from the 2MASS catalogue (Schneider et al. 2011). The dashed line is a line of equivalence. The solid line is linear fit to the data with the form $A_K = 1.63\ Av^{0.99 \pm 0.06}$.

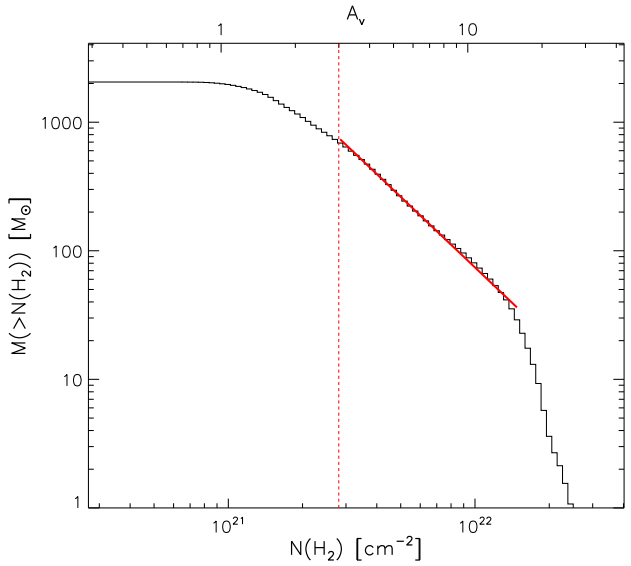

Figure 4. A cumulative histogram of mass in the 36 arcsec resolution $N(\mathrm{H_2})$ map showing the total amount of mass above a given column density threshold. The equivalent optical extinction A_V is shown by the top axis. The red line gives a best-fitting power-law index of -1.82 ± 0.02. The vertical dashed red line shows the break at $A_V = 3$ mag.

Montillaud 2013; Juvela, Malinen & Lunttila 2013). Nevertheless, the ability to obtain an estimate on these scales outweighs these factors and gives us an essential tool for enhancing our extraction of compact objects.

4.2 Total mass in the region

Fig. 4 is a cumulative mass histogram showing the total mass in the region above a given column density threshold. The total mass sampled in the map is 2000 M$_\odot$. It can be seen that there is a break in the slope of the histogram below $A_V = 3$ mag (shown by the vertical dashed red line). Above this break, the trend can be best fitted with a power-law of $\log M[< N(\mathrm{H_2})] \propto (-1.82 \pm 0.02) \log \mathrm{H_2}$. Its index of -1.82 is comparable to that of -1.9 found in Aquila (Könyves et al. 2015). The mass above $A_V = 3$ mag is 690 M$_\odot$ (34 per cent of the region total). For comparison, the mass above $A_V = 7$ mag, a value sometimes taken as a threshold for star formation (Lada, Lombardi & Alves 2010), is 160 M$_\odot$ (∼8 per cent of region total).

4.3 Power spectrum

Fig. 5 shows the power spectrum of the 500-μm resolution *Herschel*$N(\mathrm{H_2})$ column density map (solid black line). This power spectrum been corrected for the level of the noise power spectrum (by subtraction) and the *Herschel* beam (see Miville-Deschênes et al. 2010, for more details). Brunt (2010) identified a break at ∼1 pc in the power spectrum towards Taurus, which they associated with the anisotropy of Taurus on large scales. Given this break, we fit the power spectrum shown in Fig. 5 on scales beneath it with a power-law of the form $P(k) \propto k^{\gamma}$ where the best-fitting value of γ is -2.97 ± 0.02. This value broadly agrees with the value of -3.1 found by Brunt (2010) over similar scales.

Also shown in Fig. 5 is a power spectrum of the *Planck*$N(\mathrm{H_2})$ column density (blue curve) over the same area as the *Herschel* data. The spectrum has been corrected for the noise-level on the map and the instrumental beam (assumed to be a 5 arcmin HPBW Gaussian). This power spectrum closely matches that from *Herschel*, including the dip away from the best-fitting power-law on scales below k∼0.01 arcmin^{-1} (above 1 pc). The fact that this dip is seen in both spectra indicates that the cause is something common to both of them.

Analysis of *Herschel* observations shows that filaments in star formation regions have a narrow range of widths, centred on a characteristic mean width of 0.1 pc (Arzoumanian et al. 2011, 2019; André, Palmeirim & Arzoumanian 2022). We detect no break in the *Herschel* power spectrum on scales comparable to with scale. The lack of break agrees with the work of Roy et al. (2019) who showed that even if it is present the amplitude of these filaments is too low to be detected.

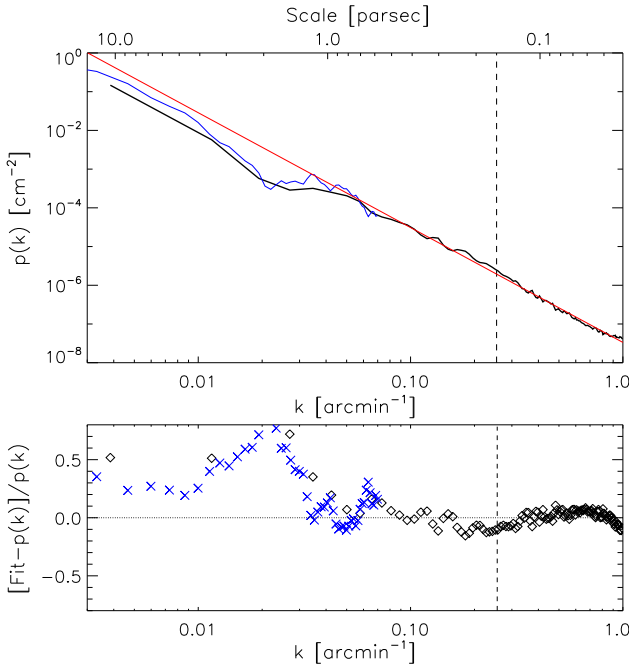

Figure 5. (*Top*) The $N(H_2)$ power spectrum towards the TMC1 region. The horizontal axis shows the wave number k and the vertical axis shows the amplitude of the spectrum $p(k)$. The black *Herschel*$N(H_2)$ spectrum has been corrected for the instrumental beam and the level of noise in the field (Miville-Deschênes et al. 2010). The red line is a power-law fit to the data on scales smaller than 1 pc (see text for details). The blue curve shows an equivalent power spectrum over the same area calculated from the *Planck*$N(H_2)$ data and assuming a Gaussian 5 arcmin beam HPBW. (*Bottom*) The residuals of $p(k)$ minus the best-fitting power-law. *Herschel* residuals in black; *Planck* residuals in blue. The vertical dashed line shows the equivalent frequency where features of size 0.1 pc should appear if they are of sufficient amplitude (Panopoulou et al. 2017; Roy et al. 2019).

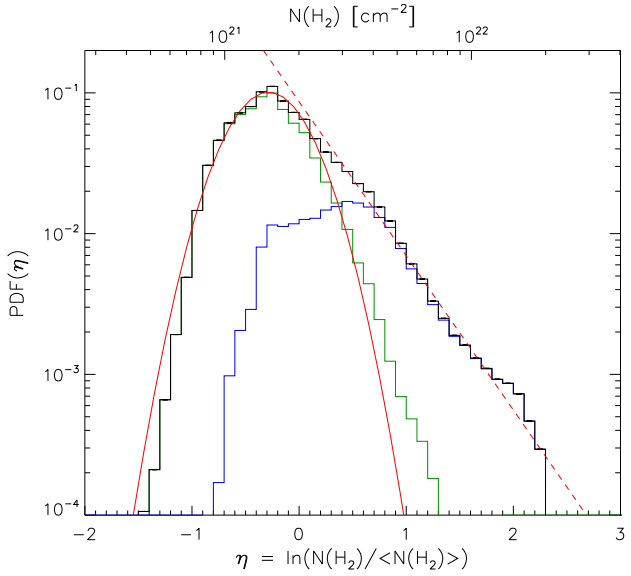

Figure 6. Probability density function (PDF; solid black line) calculated from the *Herschel* column density map of the TMC1 region. The solid red curve shows a lognormal fit to the peak of the data with a best-fitting width of $\sigma = 0.34$. The dashed red line shows a power-law fit to the high-density part of the PDF with a best-fitting index of $s = -2.48$. The solid blue line shows the PDF of the TMC1 region alone (shown by the white box in Fig. 2). The solid green line shows the PDF of the region outside of this box.

4.4 Column density probability density function

The probability density function (PDF) of column density in the TMC1 region studied in this paper is plotted in Fig. 6 as the solid black line. This effectively shows the number of sight-lines (pixels) through the TMC1 cloud with specific column densities (parametrized as the log of the mean column density). The area under the PDF is normalized to one. The plot shows the characteristic lognormal distribution with a power-law tail at higher column densities (Schneider et al. 2013; Lombardi, Alves & Lada 2015; Schneider et al. 2015). To characterize this shape, we fit the lognormal distribution below $\eta \leq 0.2$ with the form

$$\mathrm{PDF}(\eta) = \frac{1}{\sqrt{2\pi\sigma^2}} \exp\left(\frac{-(\eta - \eta_0)}{2\sigma^2}\right) \quad (1)$$

where $\eta = \ln(N(H_2)/ < N(H_2) >)$, σ is the width of the PDF, and η_0 is its central position. The best fit, shown by the solid red curve on Fig. 6, returns a value of $\sigma = 0.34$.

The higher η part of the PDF can be fit with a power-law of the form PDF $\propto N(H_2)^s$ with a best-fitting index of $s = -2.48 \pm 0.06$ shown by the dashed red line. If a region can be considered a single structure, then the power-law index s is related to the form of a radial density profile $\rho \propto \eta^{-\alpha}$ by the relation $\alpha = 1 - 2/s$ for a spherical distribution (Federrath & Klessen 2013). The fitted s thus implies a radial profile with an index of $\alpha = 1.8$. Alternatively, for a cylindrical distribution, the relation is $\alpha = 1 - 1/s$, which gives a profile index of $\alpha = 1.4$.

To examine the physical origins of the different parts of the PDF, we split the column density map into the region associated with HCL2 (the region contained with the dashed box in Fig. 2) and the material outside of that region (the area outside of the dashed box). The HCL2 PDF is shown in Fig. 6 as the blue curve while the green curve shows the PDF of material excluding HCL2. The former follows the previously fit power-law. Meanwhile, the latter closely follows the previously fitted lognormal curve with only minimal deviation at the higher densities.

4.5 Cloud structure

In Section 6, we investigate the population of dense prestellar cores in the TMC1 region. These should appear in the maps as compact sources. Fig. 7 shows a tree (a dendrogram) of structure in the TMC1 region created from the $N(H_2)$ column density map using the CSAR source extraction algorithm (Kirk et al. 2013). The dendrogram is a symbolic representation of the structure in the region. The horizontal lines are closed isocontours, and the vertical lines show the contrast between that contour and the contour level at which that region becomes substructured. Upward stems that are not terminated by a horizontal line are sources which do not contain resolved substructure.

The rms across visually flat, ∼12 arcmin-wide regions of the $N(H_2)$ map is $0.07 - 0.09 \times 10^{21}$ cm^{-2}. Therefore, we adopted for the decomposition shown in Fig. 7 a conservative σ of 0.09×10^{21} cm^{-2}, a minimum peak-to-edge contrast of three times this, and a minimum resolution (i.e. source size) equal to the HPBW of the telescope beam at 500 μm.

We find a total of 265 unstructured sources. These are enumerated by the dimensionless index (horizontal axis of Fig. 7). The main structure in HCL2 appears as a network of branches above ∼2 ×

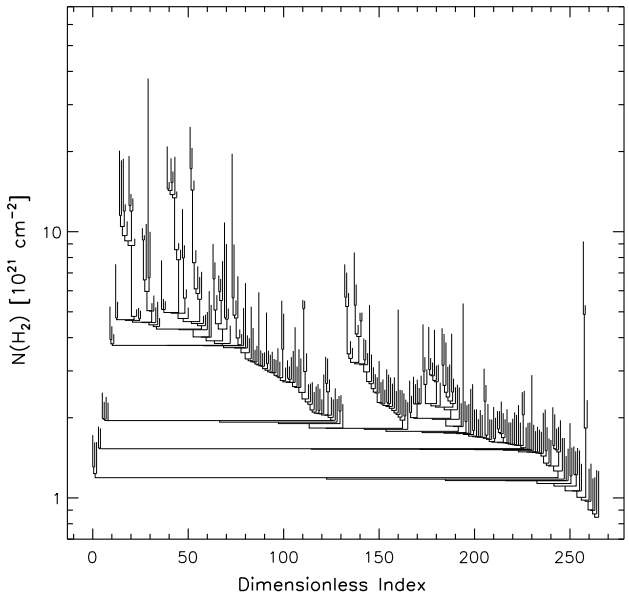

Figure 7. A dendrogram of the $N(H_2)$ column density map towards the TMC1 region created with the CSAR algorithm (Kirk et al. 2013). Horizonal lines are closed contours around resolved features with a minimum density contrast (3 σ), vertical lines show the contrast between contours and their substructure. Upward lines without a capping horizontal are sources which have no resolved substructure.

10^{21} cm^{-2} between indices of ∼ 10 and 130. Examining the column density values in Figs 6 and 4, we see that $\sim 2 \times 10^{21}$ cm^{-2} is approximately the same column density where the PDF transitions from lognormal to linear and where the linearity of the cumulative histogram breaks down.

There are also hundreds of single-leaf branches that merge consecutively with the larger trees (e.g. the pattern around index 100 or 299–260). These branches correspond to minor cirrus and background features with little or no organized substructure.

5 FILAMENTARY STRUCTURE

5.1 Extracting filaments

One of the major features of the *Herschel* era has been interest in filamentary modes of star formation (e.g. André et al. 2014; Arzoumanian et al. 2019; Schisano et al. 2020). There are several topological methods for tracing filamentary structures in maps. We have used here the DISPERSE software package to trace filamentary structures in the $N(H_2)$ map of the TMC1 region.

The DISPERSE package traces persistent structures by connecting critical points, e.g. maxima, saddle-points, and minima in a 2D map, with integral lines, e.g. tangential paths to the local gradient (Sousbie 2011). Key to this concept is persistence, i.e. the minimum allowed contrast between two connected critical points. Arzoumanian et al. (2019) examined the input parameters with respect to *Herschel* maps and recommended a persistence value on the order of the background rms on the map.

Fig. 8 shows the results for running DISPERSE on the low-resolution $N(H_2)$ map. We adopt a conservative persistence threshold of 0.09×10^{21} cm^{-2}, equal to the rms used for the CSAR decomposition in Section 4.5. We follow Arzoumanian et al. (2019) in using an assembly angle of 50°, a smoothing kernel of twice the map resolution and a minimum background contrast of 2×10^{21} cm^{-2}, i.e. 1.5× the mean background where the rms was measured. Features shorter than 10 times the map resolution (360″, ∼ 0.25 pc @ 140 pc) were removed from the network, leaving a total of 53 filaments.

Filaments were identified in the lower resolution (36 arcsec) column density map, but features were then measured from the higher-resolution (18 arcsec) map. For example, median radial profiles were constructed for each filament using the skeleton data from DISPERSE's run. The orientation of the filament at each critical point was calculated by averaging the angle of the skeleton segments before and after it. A profile of the pixels orthogonal to this angle was extracted for each side the filament at the node. The median profile on each side of the filament was then taken, the dispersion at each point being the median deviation from the median profile.

Integrating across the filament profile gives $M_{\rm line}$, the mass per unit length of the filament. The critical $M_{\rm line}$ for an isothermal cylinder to be thermally stable against axisymmetric perturbations is

$$M_{\rm line,crit} = \frac{2c_{\rm s}^2}{G} = \frac{2k_{\rm B}T}{G\mu m_{\rm H}}, \quad (2)$$

where $c_{\rm s}$ is the sound speed, G is the Gravitational constant, T is the gas temperature, μ is the mean mass per particle, and $m_{\rm H}$ is the mass of a hydrogen nucleus (Inutsuka & Miyama 1997). For typical molecular weights (μ = 2.37, e.g. Kauffmann et al. 2008) and temperatures (T = 10 K) in molecular star formation regions, the critical line mass is 16.2 $M_\odot$/pc. We check the mean mass per unit length of each filament against this value to test each filament's stability.

The 53 filaments were then filtered via the robustness criterion listed in Arzoumanian et al. (2019), namely that the filaments have an axis ratio (length divided by Gaussian full width at half-maximum, FWHM) greater than 3 and a background-to-filament amplitude contrast greater than 0.3. This final cut left 35 robust filaments out of 53. The robust filaments are shown in Fig. 8. These are colour coded to match the Arzoumanian et al. (2019) descriptions of thermally supercritical, transcritical, and thermally sub-critical against the critical mass to unit length. The single longest supercritical filament shown in Fig. 8 is the TMC1 filament (it is annotated). This filament corresponds to an ∼ 11 K linear feature in Fig. 2, demonstrating that it is one of the coldest and densest features in the TMC1 region. Fig. 8 also illustrates that most of the other filaments in the TMC1 region are sub-critical filaments that generally appear at lower background column densities.

5.2 Filament widths

The filament profiles exhibit a range of morphologies. The centres are broadly Gaussian, but a number of them depart from that shape in their outer parts and are better fit with a Plummer-like profile. To gauge the $FWHM$ of the inner part of the filament, we follow Arzoumanian et al. (2019) by fitting a Gaussian to the profile within 1.5 × HPHW of the centre, where the $HPHW$ is the point where the filament profile has dropped to half the peak amplitude measured above the background. The effective beam $FWHM$ of the map is subtracted in quadrature from the fitted Gaussian to give a deconvolved filament width, $FWHM_{\rm dec}$.

The histogram of measured $FWHM_{\rm dec}$ is shown in Fig. 9. The width of each filament is determined twice using each side of the median profile of the filament independently. The distribution of the 'left-hand' and 'right-hand' fits is shown in Fig. 9. The distribution of averaged $FWHM_{\rm dec}$ for all robust filaments is also shown. This latter histogram shows a peak at ∼ 0.07 pc, identical to the the peak in the filament width distribution found in the neighbouring B211/213

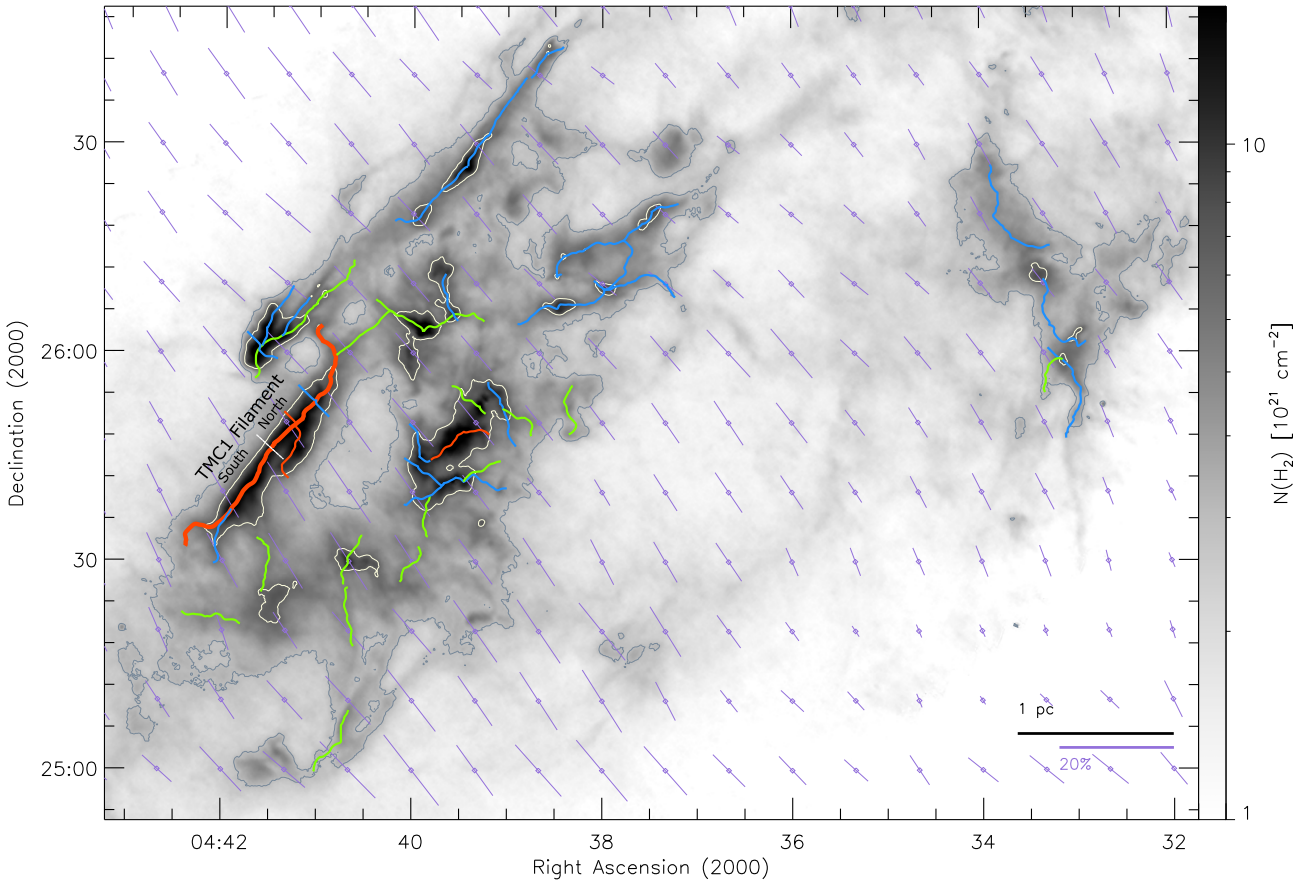

Figure 8. The filamentary network towards the TMC1 region as traced by DISPERSE plotted over the $N(H_2)$ map. The red, blue, and green lines denote filaments that are supercritical, trans-critical, and subcritical against axisymmetric perturbations, respectively (see text for details). The purple vectors show the magnetic field direction inferred from the 353 GHz *Planck* polarisation data. Distance and percentage polarisation reference bars are shown in the bottom-right corner. The grey and white contours denote column densities at the equivalent of an A_V of 3 and 7 mag, respectively. The TMC1 Filament is annotated and shown by a thicker line weight, and a short white orthogonal line shows the split between the North and South sections.

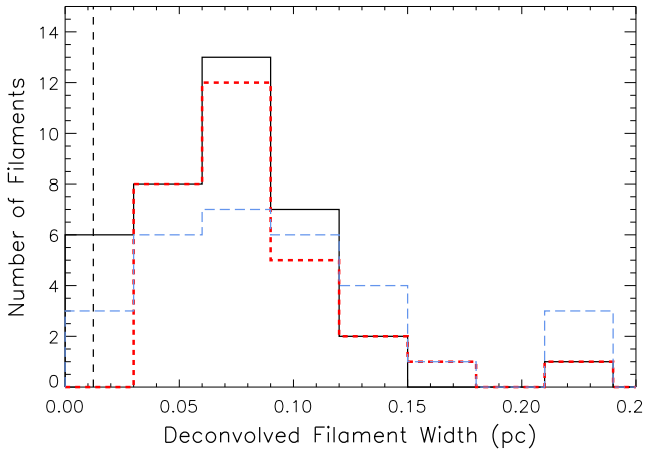

Figure 9. The distribution of deconvolved full width at half-maximum (FWHM) widths from Gaussian fitting to the inner part of each filament. The red dotted and blue dashed curves show the widths derived from the separate 'left' and 'right' fits for each filament. The black curve shows the FWHM averaged between left and right for each filament. The vertical black dashed line shows the effective FWHM of the map. The FWHM were fitted on the high-resolution (18 arcmin) column density map.

region (Palmeirim et al. 2013). As discussed in André et al. (2022), width estimates based on Gaussian fits are typically underestimated in the presence of significant power-law wings, and the deconvolution of widths at larger distances can make it hard to interpret filament FWHMs. However, the effective FWHM used for deconvolution (vertical line in Fig. 9) is sufficiently small for these observations not to make an appreciable difference. Based on a Plummer-fit analysis, the TMC1 filament itself has a mean half-power width of ~ 0.13 pc (see Section 5.4 below).

5.3 Filament orientation

We compare the orientation of the TMC1 regions filaments with the larger-scale magnetic field direction inferred from the Planck 353 GHz polarisation products (Planck Collaboration XI 2020). The purple vectors in Fig. 8 show the directions of the larger-scale magnetic field so determined. The field is broadly uniform across the TMC1 region but does bend slightly. The majority of supercritical filaments appear to be orthogonal to the field direction.

We define the orientation of a filament as the median position angle across its nodes. The normalized distribution of mean position angles is shown in Fig. 10. The relative distribution for supercritical filaments occupies a narrow position angle range with values of approximately $-50 - 0^{\circ}$. The normalized orientation of the magnetic field vectors from Fig. 8 is also shown. There is a clear offset between

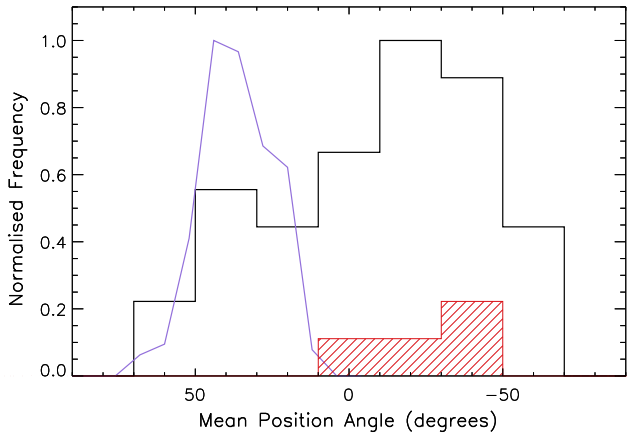

Figure 10. Comparison of filament position angles to the magnetic field direction. The black curve shows the histogram of all robust filaments towards the TMC1 region. The red shaded histogram shows the orientation of supercritical filaments. The purple curve shows the normalized histogram of the magnetic field direction across the map sampled on a 1 arcmin scale. Both red and black histograms are normalized to the peak of the black histogram.

these two position angles of approximately 90° degrees, showing that the supercritical filaments are orientated orthogonal to the magnetic field direction. This result is similar to that of Palmeirim et al. (2013) who found that the main supercritical filament in the L1495 region was also aligned orthogonal to its local magnetic field direction.

5.4 The TMC1 filament

The TMC1 filament is a thermally supercritical filament that runs in a north-westerly direction from an RA of 04:42 and Dec. of +25:35 to an RA of 04:41 and Dec. of + 26:00, as shown and annotated in Fig. 8. This filament is heavily studied as a prototypical chemically young star-forming site (McGuire et al. 2018; Soma et al. 2018; Fuente et al. 2019). The DISPERSE extraction split the TMC1 filament in two at a Declination of + 25:47:45. We refer to the two parts as the 'North' and 'South' TMC1 filament, each of which has a length of 0.9 pc. Note that the North and South filaments respectively correspond to the distinct Planck Galactic Cold Clumps G174.20-13.44 and G174.40-13.45 (Fehér et al. 2016; Planck Collaboration XXVIII 2016).

As noted earlier, Nutter et al. (2008) found that the TMC1 filament (the 'Bull's Tail') was consistent with a narrow, cold (∼ 8 K) core and a broader, warmer (∼ 12 K) jacket. The *Herschel* emission is a product of dust at different temperatures along the line of sight so the single temperature estimated from it will be a characteristic average. Nevertheless, the Bull's Tail is prominently shown as a cold feature (the red strip in Fig. 2). The filament is sufficiently dense to have been seen in absorption in a *Spitzer* 70 μm map (Nutter et al. 2008), as discussed in Section 4.1.

The median profiles for the North and South filaments are shown in Fig. 11. The profiles have been reconstructed and analysed independently on each side of each filament, following the approach and conventions of Arzoumanian et al. (2019). Both filaments run in a broadly SE–NW orientation. Therefore, the left hand profiles in Fig. 11 correspond to the NE side of the filaments, whereas the right hand profiles correspond to the SW side. For simplicity, we refer to these as the 'left' and 'right' profiles.

Fig. 11 shows the median profile along the filament and the median dispersion around the median profile. In addition, the best-fitting Gaussian profile to the inner part of the profile is shown (see Section 5.2). The South filament (both sides) and the left North filament have $FWHM_{\rm dec}$ approximately equal to the peak of 0.07 pc shown in Fig. 9, but the right North filament has a larger $FWHM_{\rm dec}$ of 0.12 pc. The North filament is relatively well fit by a Gaussian profile out to large radii, albeit at a cost of poor constraint on peak. By contrast, the South filament is well fit on peak, but its greater peak-to-background contrast more readily shows a departure from the Gaussian profile.

An estimate of the outer width of each profile can be made as the place where the gradient of the smoothed profile goes to zero (see Arzoumanian et al. 2019 for details). This point is shown in each case also in Fig. 11. The level of the profile at this point it taken as the profile background. The North filament appears broadly symmetric with similar background levels and widths on either side. The South filament, however, appears more asymmetric with a high background on the left and a low background on the right as it tapers away into the noise. The mean background level of the first three is $\sim 3 \times 10^{21}$ cm^{-2}, but is only half that for the last one. This difference can be seen in Fig. 8 by the empty space between the filament and the edge of the figure. The North filament and the left profile of the South filament have widths of ∼ 0.3 pc. The right profile of the North filament, however, has a width of twice this at 0.7 pc, again, most likely due to the lack of other features surrounding it.

The North filament has a mean column density of 6.5×10^{21} cm^{-2} whereas the South one has a mean of 13×10^{21} cm^{-2}. This difference is consistent with maps of molecular line emission that show stronger integrated emission from the South filament (e.g. Fehér et al. 2016; Dobashi et al. 2018).

A Plummer-like profile of the form:

$$N_{\rm H_2}(r) = N_{\rm H_2}(0)\left(1 + (r/R_{\rm flat})^2\right)^{-\frac{p-1}{2}} \quad (3)$$

was fitted to the background-subtracted profiles where $N_{\rm H_2}(0)$ is the peak of the profile, $R_{\rm flat}$ is the approximate radius of the central region of constant column density, and p is the power-law exponent of the column density profile at large values of r. Fig. 11 shows the best Plummer-like profile fit to each profile. The power-law exponents for all four profiles are in the range 1.6–2.6. Notably, the most 'featureless' profile (lower right) has an exponent closest to 2 ($p = 1.9$). The North and South part of the TMC1 filament have mean half-power widths from the Plummer fits ($2\sqrt{3}R_{\rm flat}$) of 0.20 and 0.06 pc, respectively, the mean of these is ∼ 0.13 pc. This does agree with the visual inspection of Figs 8 and 11 as there does appear to be more material around the Northern filament.

The North filament has a mean $M_{\rm line}$ of 38 M$_\odot$/pc and the South filament a mean $M_{\rm line}$ of 69 M$_\odot$/pc. These values make them respectively three and five times thermally supercritical. These values are slightly higher than, but still consistent with, those found by Fehér et al. (2016). Fig. 12 shows the location of dense cores in TMC1 (see next section). Interestingly, the North filament is associated with 6–7 dense cores, whereas the more thermally supercritical South filament is only associated with 1–2 dense cores. In both cases, only one core in each set is prestellar in nature (see the following section for methodology). Zeeman measurements towards the South filament suggest that it is magnetically marginally supercritical as well, with a mass-to-flux ratio of 2.2 (Nakamura et al. 2019).

Different velocity components have been detected within the entire TMC1 filament (Fehér et al. 2016; Dobashi et al. 2018). These components have been interpreted as sub-filaments whose mass-per-unit length still exceeds thermal supercriticality (Fehér et al. 2016; Dobashi et al. 2018). The TMC1 filament therefore appears to be

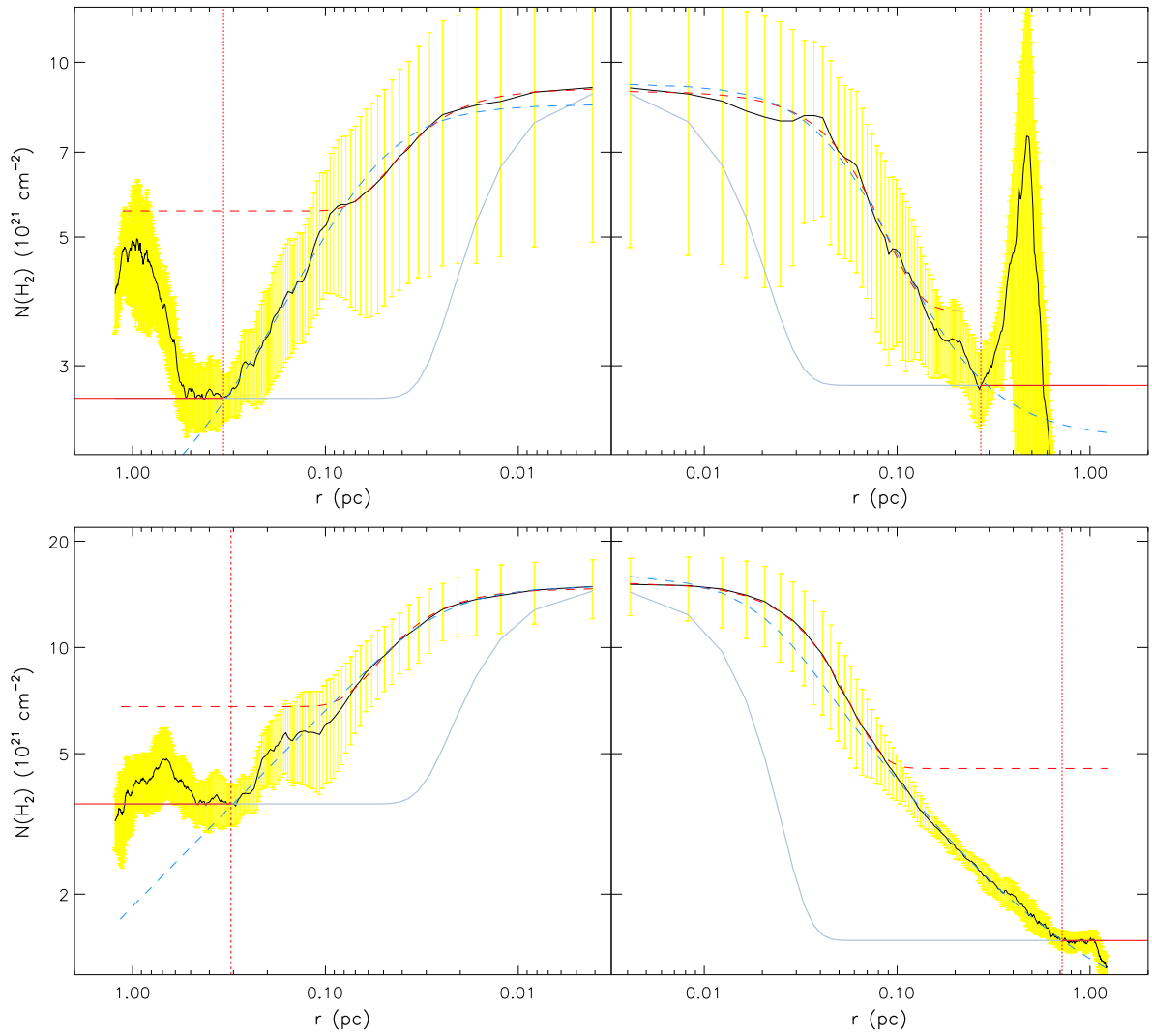

Figure 11. Median left (NE) and right (SW) column density profiles of the North and South parts of the TMC1 filament as measured from the high-resolution (18 arcmin) column density map. Properties and fits are done independently for each side of each filament. The black curve is the median column density profile itself and the yellow bars are the median dispersion along the length of the profile at that radius. The red dashed curve is a Gaussian fit to the inner profile. The horizontal solid red line is the background column density level (where the smoothed gradient of the profile is approximately zero) and the vertical dotted line is the filament width at this background level. The dashed blue line is a best-fitting Plummer-like profile. The thin blue line is the resolution of the column density map. See text for full details.

poised for collapse, with the North filament already having formed several dense condensations but the South filament still relatively undifferentiated with only a couple of dense condensations. This behaviour is consistent with the idea of TMC1 being a chemically young star-formation site (e.g. McGuire et al. 2018; Soma et al. 2018; Fuente et al. 2019).

6 DENSE CORE CATALOGUE

6.1 Catalogue creation

The dendrogram in Fig. 7 and the filament maps in Fig. 8 show that the dense cores in the TMC1 region are part of a complex tree of emission from which they need to be separated. For the creation of a dense core catalogue, we use the GETSOURCES source extraction package which can separate blended sources and work simultaneously across multiple wavebands (Men'shchikov et al. 2012).

In brief, GETSOURCES spatially decomposes the emission in a map into a series of strongly filtered 'single-scale' images. A source is then identified on the smallest spatial scale and tracked through larger spatial scales until it reaches some maximum specified size, or its surface brightness becomes too low to be detected (Men'shchikov et al. 2012). The software is run in two passes – the first for detection, the second for measurement. Decomposing a set of observations in this manner allows equivalent spatial scales from multiple wavebands to be correlated together during the actual extraction process and thus eliminates the need to cross-match independent monochromatic catalogues after the fact (Men'shchikov et al. 2012).

The HGBS was primarily designed to take a census of cold starless cores which primarily emit at longer wavelengths (160–500 μm) and embedded YSOs and protostellar cores which also emit at shorter wavelengths (e.g. 70 μm). It was therefore necessary to create two source extraction forks optimized for these two classes

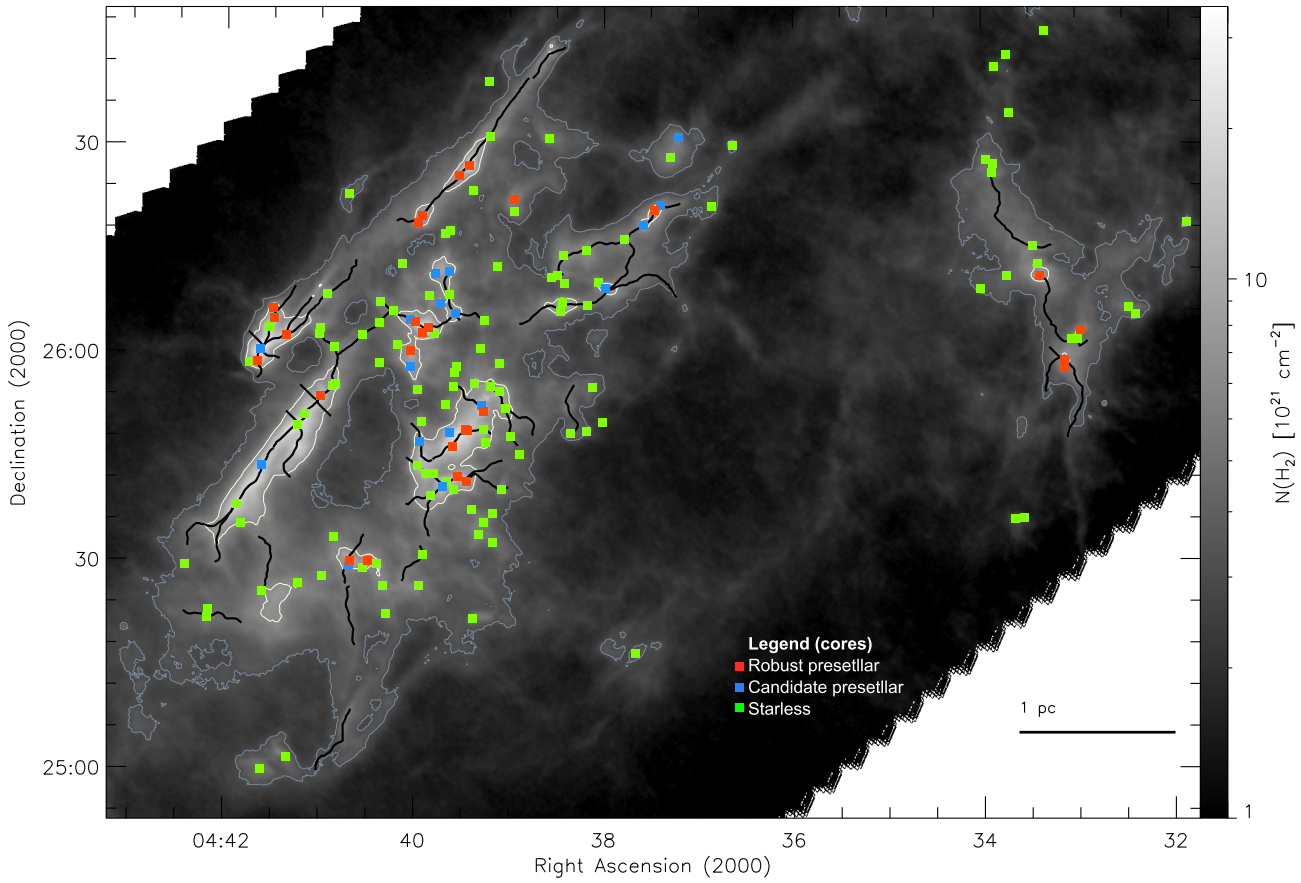

Figure 12. The location of starless and prestellar cores overplotted on the $N(H_2)$ map. The red, blue, and green markers show the respective locations of robust prestellar, candidate prestellar, and starless cores. Two contour levels, $A_V = 3$ and 7, are shown for comparison. The network of filaments from Section 5 is also shown for comparison.

of object. Version v1.140127 of GETSOURCES was used. The HGBS catalogue creation procedure is described in full in Könyves et al. (2015).

A common extraction was performed up to the detection stage on flattened backgrounds. The first extraction fork created an extended source catalogue by using the 160–500−μm maps for source selection. The second extraction fork created a 70-μm-identified compact source catalogue using only the 70-μm map for selection. For both catalogues, photometry was performed at 70–500 μm. The extractions' focus on the dense material was enhanced by using the high-resolution column density map as a pseudo-wavelength, and a temperature-corrected 160-μm map. These weighted the extraction towards sources of high column density rather than just high surface brightness.

Fifty-five sources were extracted in the compact source pass, and 510 were extracted in the extended source pass. Of those, 45 and 285 were defined as acceptable, respectively, based on their global detection significance (GOOD = 1, see Men'shchikov et al. 2012 for details). GETSOURCES separates the detection significance of extraction from the photometric significance of the resulting measurements. These are respectively SIG_MONO (the best signal-to-noise on a single spatial scale) and SNR_MONO (the traditional photometric signal-to-noise).

A set of selection rules was applied to each of the photometric catalogues to create science catalogues. A catalogue of dense core candidates was created by filtering the extended source catalogue for sources that:

(i) were detected (SIG_MONO> 5) in at least two wavelengths and the $N(H_2)$ map,

(ii) had reliable flux measurements (SNR_MONO> 1) in at least one wavelength and the $N(H_2)$ map,

(iii) and a detection significance summed over all wavelengths of at least 10.

These filters produced a catalogue of 201 objects. These sources were visually inspected, and 23 entries (11 per cent) were rejected, leaving a final catalogue of 178 dense core candidates.

The robustness of these dense core candidates was assessed by comparing the GETSOURCES extraction to the results of a CSAR extraction performed on the high-resolution column density map. We find that 48 per cent of sources in the extended source catalogue matched a CSAR position within their $N(H_2)$ FWHM contour, and a further 33 per cent of starless core candidates matched a CSAR core. These percentages are typical of those found in other clouds.

Starless cores are pockets of molecular gas that do not have embedded protostellar sources. The dense core catalogue was filtered for these by comparing it against the compact 70-μm source catalogue from the compact extraction, the *Spitzer* Taurus YSO catalogues of Rebull et al. (2010), and the NED Extragalactic database (Helou et al. 1991). In all cases, a match was found if external catalogue coordinates were found to lie within the half-power ellipse of a dense core in the high-resolution $N(H_2)$ map. A total of eleven sources, 10 YSO candidates, and one galaxy, were rejected by this process, leaving a final catalogue of 167 starless core candidates.

6.2 Core properties

The properties of TMC1 region starless cores are listed in Table B1 and their locations are shown in Fig. 12

We define two radii for the cores. The raw radius of the core is the geometrical average of the major and minor FWHMs of the core in the high-resolution column density map, $\overline{FWHM}$. The deconvolved radius is then calculated as $R_{\rm decon} = \sqrt{\overline{FWHM}^2 - \overline{HPBW}^2}$ where $\overline{HPBW}$ is the resolution of the high-resolution column density map (18.2″).

The temperatures and masses of the starless cores were estimated by fitting their integrated flux SEDs between 160 and 500 μm in the same manner used for the creation of the column density map (see Section 4.1 for details). Following Könyves et al. (2015), the quality of the fit was checked by fitting a second permutation of the SED using the wavelengths 70–500 μm and by weighting via the detection significance rather than the measurement errors. SED results were accepted if the two mass estimates were within a factor of two of each other, at least three bands were used to fit the SED, and the integrated flux at 350 μm was higher than that at 500 μm. This process left 59 per cent of the cores with a valid SED, i.e. 96 cores. A temperature equal to the median temperature of cores with valid SEDs is assumed for cores without a valid SED (see Section 6.4).

6.3 Prestellar cores

Starless cores which are likely to be taking part in the star formation process are termed prestellar (i.e. they have some signs of being gravitationally bound). An estimate of the stabilities of the cores can be made by comparing their masses to that of a critical Bonner–Ebert (BE) sphere (Ebert 1955; Bonnor 1956). A BE sphere is a pressure-confined isothermal sphere of gas that will be unstable against collapse if its mass is above a critical value given by

$$M_{\rm crit} = 2.4\frac{Rc_{\rm s}^2}{G} \tag{4}$$

when the sound speed is given by

$$c_{\rm s}^2 = \frac{k_{\rm B}T}{m_{\rm H}\mu} \tag{5}$$

and R is the sphere's radius, and the other values are as defined earlier. We estimate $M_{\rm crit}$ for each core using its deconvolved radius for R and its catalogue temperature for T.

Following Könyves et al. (2015) and with analogy to the virial ratio, we classify a starless dense core as a robust prestellar core if the ratio $\alpha = M_{\rm crit}/M_{\rm core}$ is ≤ 2. In practice, marginally resolved cores will have a significant error in R. Therefore, following Könyves et al. (2015) and Paper I, we adopt a size-dependent threshold given by $\alpha \leq 5 \times (\overline{HPBW}/\overline{FWHM})^{0.4}$ where $\overline{HPBW}$ is the map resolution and $\overline{FWHM}$ is the mean undeconvolved source radius (see above) measured in the high-resolution $N(\rm H_2)$ map. Cores that meet this second criterion but not the first are classified as candidate prestellar cores.

Out of the catalogue of 167 starless cores, 27 were classified as robust prestellar cores, and a further 17 were classified as candidate prestellar cores. Fig. 12 shows the location of the starless, candidate prestellar, and robust prestellar cores. As shown by the extinction contours, most of the robust and candidate prestellar cores appear at locations with a column density higher than $A_V = 5 - 7$ and close to the location of filaments.

Fig. 13 shows a plot of deconvolved core radius versus mass for all cores towards the TMC1 region. The unbound starless cores cluster towards the lower part of the diagram and are coincident with the yellow band which shows the mass–size correlation observed for diffuse CO clumps (Elmegreen & Falgarone 1996). The robust prestellar cores and candidate prestellar cores, however, have relatively higher masses.

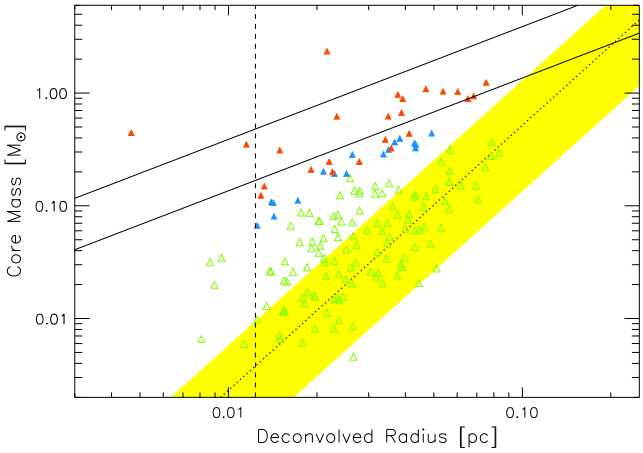

Figure 13. Core mass versus size for the population of starless cores towards the TMC1 region. The green symbols show unbound starless cores, the blue symbols candidate prestellar cores, and the red symbols show robust prestellar cores. The size is taken as the deconvolved radius from the high-resolution column density map while the mass is the mass from greybody fit to the integrated fluxes of the cores. The yellow band and the dotted line shows the expected mass–size relationship for diffuse CO clumps (Elmegreen & Falgarone 1996). The solid lines show the expected mass–size relationship for 7- and 20-K Bonner–Ebert spheres.

6.4 Temperature and density of cores

The left-hand side of Fig. 14 shows the distribution of temperatures from (valid) core SEDs for starless cores and prestellar cores. The median value of their combined distribution is 11.4 ± 1.4 K. This temperature is virtually identical to that found by Könyves et al. (2015) for Aquila cores when they first used this technique. For cores without a valid SED fit, we estimate a mass from their longest significant wavelength assuming a dust temperature equal to this median. Fig. 14 also shows the distribution of pixel-by-pixel temperatures in the map of SED dust temperatures (i.e. Fig. 2). The median value of this distribution is 15.0 ± 0.8 K. These temperatures are generally higher than those for individual cores as the warmer inter-core medium dominates the latter distribution. The background flux around each core, including the contribution from the warmer dust, is subtracted from the cores by GETSOURCES before SED fitting.

For each core, we also fit its background-subtracted peak intensity at a common HPBW (equivalent to that at 500 μm) to estimate the peak column density in the core. These peak column density estimates are plotted on the right-hand panel of Fig. 14. Shown here are the pixel values from the 500 μm resolution column density map and the fitted peak values from the cores. This panel shows that prestellar and unbound starless cores have distinctly different peak densities with a break at approximately $3 - 4 \times 10^{21}$ cm^{-2} ($A_V \sim 3$ mag). This column density is approximately the same as the break seen in the cumulative core mass function and the transition between the lognormal and power-law components of the PDF towards the TMC1 region.

The differential core formation efficiency (CFE) can be used to examine the density at which a cores actually forms. The CFE is the

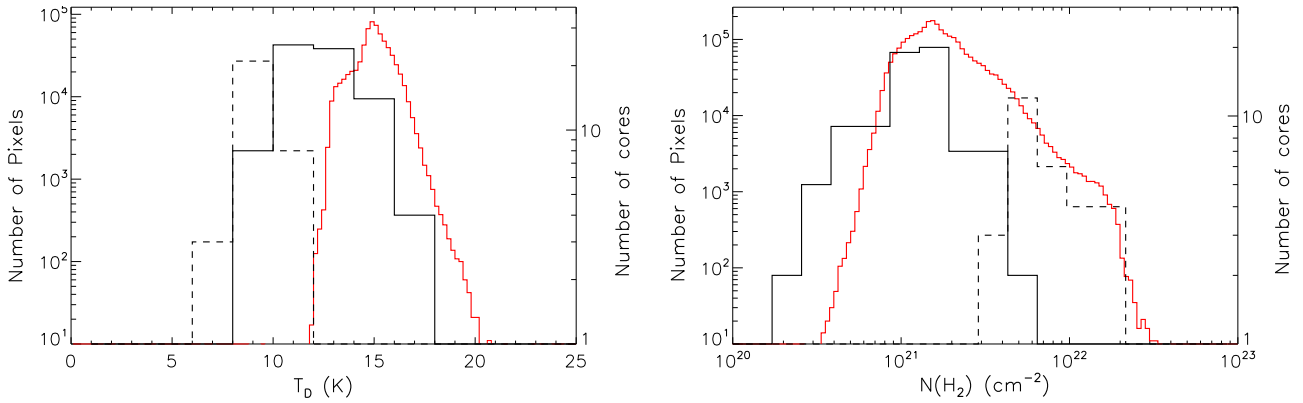

Figure 14. Histograms of *(left)* fitted SED temperatures and *(right)* core background-subtracted peak $N(H_2)$ column densities at the 500 μm resolution. The right-hand axis and the black curve on each plot show the histogram for unbound starless cores (solid line) and prestellar cores (dashed line). The left-hand axis and the red curve on each plot show the histogram of all valid pixel values in the map from Fig. 2.

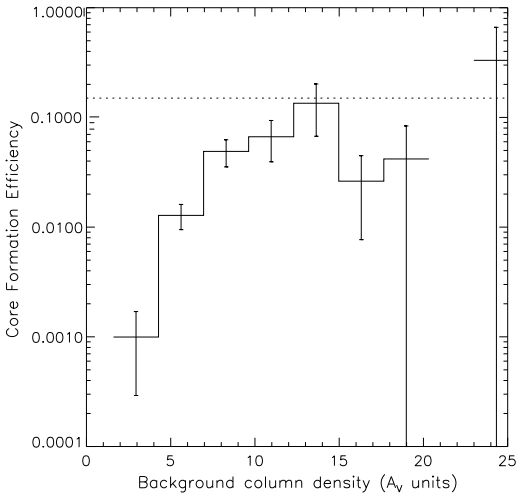

Figure 15. Core formation efficiency versus extinction. The horizontal dashed line is an efficiency of 15 per cent.

ratio of the mass of cores forming at a specific background column density to the total mass in the cloud at that column density. In the regions of Aquila, Ophiuchus, and Cepheus, the CFE peaks at around 10–15 per cent between $A_V \approx 10$ and 20 and levels off at higher extinctions (Könyves et al. 2015; Di Francesco et al. 2020; Ladjelate et al. 2020). The dependence of the CFE on background column density is very similar in all those regions. What separates them is the low-A_V edge at which they first hit 10–15 per cent. In Cepheus (Di Francesco et al. 2020), Ophiuchus (Ladjelate et al. 2020), and Aquila (Könyves et al. 2015), this is $A_V = 7$, 10, and 20, respectively. Fig. 15 displays the CFE plot for the Taurus region, showing an initial jump at $A_V \sim 5$ before reaching the 15 per cent level around $A_V \sim 14$. Thus, the TMC1 region follows the same basic trend as the other regions, but there is not enough high column density material in Taurus/TMC1 to give reasonable statistics at higher extinctions. Fig. 14 also reinforces the lack of high column density gas, and therefore the lack of cores at higher extinctions in TMC1, where the maximum column density in the region is 2×10^{22} cm^{-2} ($A_V \sim 22$).

In the TMC1 region, star formation happens like in other parts of Taurus, such as L1495, but at somewhat lower extinctions compared to other clouds such as Aquila or Ophiuchus. There is only one thermally supercritical filament and only a few transcritical filaments in the region (as seen in Fig. 8). Only 10 per cent of all filaments have an average equivalent A_v above $7-8$ mag, which is considered a density threshold for star formation. Di Francesco et al. (2020) discuss the issue of core formation at low A_V with respect to the Cepheus region and note that the relative unavailability of transcritical and supercritical filaments at lower column densities is the simplest explanation for the low number of cores. It is possible that the same bottleneck applies in the TMC1 region, given its range of column densities. Even though there are fewer supercritical/transcrital filaments, a comparison of Figs 8 and 12 does suggest that most robust/candidate prestellar cores of TMC1 lie along those filaments, in agreement with the filament paradigm of star formation (cf. André et al. 2014).

6.5 Completeness for prestellar cores

We estimate the completeness of our prestellar core extraction by performing Monte Carlo simulations following Könyves et al. (2015). The details and simulated core population are the same as used in Paper I. In brief, our detected sources were removed from the *Herschel* flux maps and a population of 267 simulated critical BE spheres were injected into that map towards regions of high column density. A full GETSOURCES extraction was then performed on the simulated maps. The completeness tests were focused on the range of masses where the completeness limit was expected to reside based on other *Herschel* studies (Könyves et al. 2015; Paper I; Bresnahan et al. 2018).

Fig. 16 shows a plot of simulated core mass versus estimated completeness. A simulated prestellar core is considered detected if its detected position matches the input position within 9″ and if it is classified as a prestellar core via the process described earlier in this Section. A total of 181 out of the 267 simulated cores were recovered and correctly classified as prestellar by this procedure. The horizontal dashed line in Fig. 16 shows the same 85 per cent completeness threshold as used in Paper I. The estimated completeness drops below this threshold consistently for simulated cores with masses < 0.06 M$_\odot$. The dotted line in Fig. 16 shows the same model for completeness as used in Paper I based on the procedure described in Könyves et al. (2015) and appendix B2 of Könyves et al. (2015).

Comparing the simulated to derived masses shows that the cores' masses are underestimated by approximately 10–20 per cent above this completeness level, albeit with considerable scatter. The standard deviation in the ratio of recovered to simulated masses settles down to 25–30 per cent for detected masses above 0.15 M$_\odot$. The value of 0.06 M$_\odot$ from the previous paragraph could show that our extraction

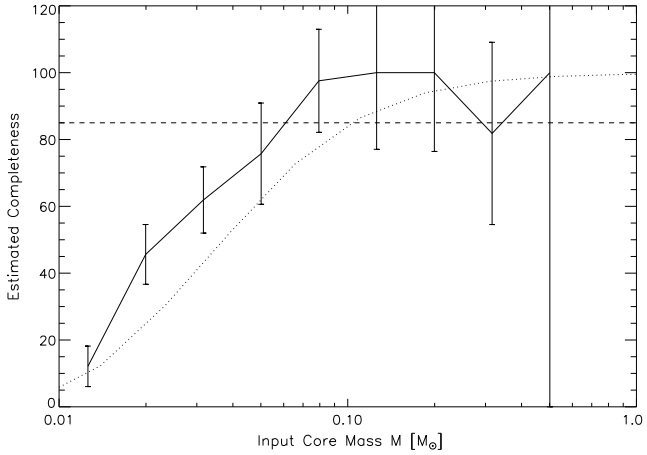

Figure 16. The fraction of recovered simulated prestellar cores versus simulated core mass. The error bars assume a Poisson distribution. The horizontal dashed line shows 85 per cent completeness. The dotted line shows the completeness model from Paper I and appendix B2 of Könyves et al. (2015).

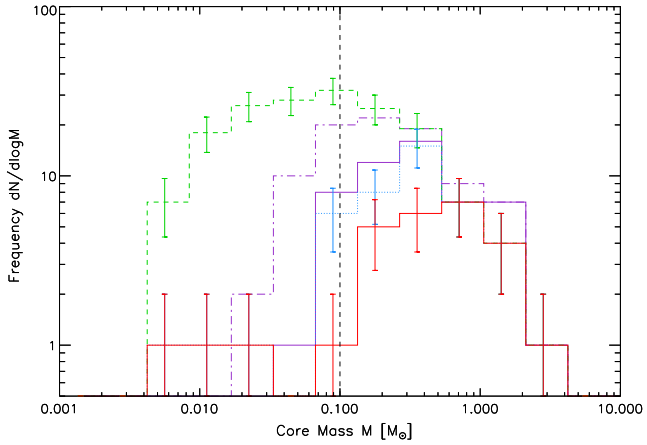

Figure 17. Histogram of starless core masses in the TMC1 region. The coloured lines denote different populations: dashed green shows all starless cores, blue dotted shows candidate and robust prestellar cores, while solid red robust prestellar cores alone. The solid and dashed purple curves respectively show the robust and candidate cores from Paper I. Error bars are shown based $\sqrt{N}$ uncertainties. The vertical dashed black line shows our 0.1 $M_\odot$ completeness limit.

went marginally deeper than that in Paper I which arrived at a completeness estimate of $M > 0.1$ $M_\odot$ for detection. The difference could be ascribed to the slightly different dynamic range of the two tiles as that is an important factor in the sensitivity of a GETSOURCES extraction. Nevertheless, we adopt a conservative completeness threshold for detection of $M > 0.1$ $M_\odot$ for consistency with Paper I and a threshold for reliable mass determination above $M > 0.15$ $M_\odot$.

6.6 Prestellar core mass function

Fig. 17 shows the core mass function (CMF) for our 44 prestellar cores (robust and candidate) and just the 27 robust prestellar cores. The median mass of the prestellar cores is 0.33 $M_\odot$. Fig. 17 also shows the CMF for all 167 starless cores in the TMC1 region. The median mass of the starless cores is 0.07 $M_\odot$, a mass just a little lower than the 0.1 $M_\odot$ completeness limit. For comparison, we also shown in Fig. 17 the CMF for cores from the neighbouring L1495 region, as extracted in Paper I. Note that L1495 contains more prestellar cores overall, largely due to the B211/213 filament and the cores associated with it.

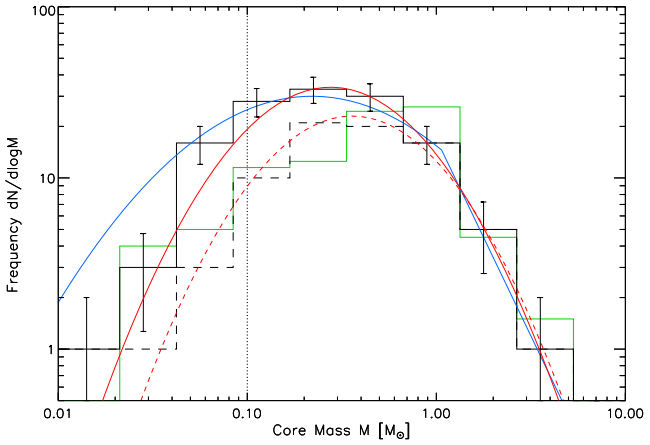

Figure 18. The combined mass function for the L1495 and TMC1 regions. The solid black line shows all prestellar cores, the dashed black line shows robust prestellar cores. The red curve shows a lognormal fit to the prestellar core distribution above the completeness limit of this paper (0.1 $M_\odot$, shown by the vertical dotted black line). The blue curve shows a scaled initial mass function (IMF) from Chabrier (2003) and the green curve shows the Taurus IMF derived by Luhman et al. (2009).

Fig. 18 shows a combined CMF for Taurus including robust and candidate prestellar cores from both TMC1 (this paper) and L1495 (Paper I). The error bars show $\sqrt{N}$ uncertainties. This curve is best fitted by a lognormal curve that peaks at 0.28 ± 0.08 $M_\odot$. The curve has standard deviation of 0.42 ± 0.06, close to the value of 0.45 found for dense cores in Aquila (Könyves et al. 2015). Also shown is the CMF for purely robust cores and an equivalent best-fitting lognormal curve. That fit peaks at 0.36 ± 0.08 $M_\odot$ and has a standard deviation of 0.40 ± 0.06.

Fig. 18 also shows a scaled version of the standard initial mass function from Chabrier (2003). Note that the initial mass function (IMF) for young stars in Taurus has been reported to differ from that seen in other regions, with an excess of stars between $0.7 - 1.0$ $M_\odot$ and a deficiency of stars above that mass (Luhman et al. 2009; Kraus et al. 2017). We therefore also show in Fig. 18 the Taurus IMF from Luhman et al. (2009). This IMF has been scaled to match the number of cores at the high mass end. The Robust CMF most closely matches shape of the Luhman et al. (2009) IMF as it peaks at a higher mass than the Chabrier (2003) IMF. Note, however, that neither the Chabrier (2003) nor the Luhman et al. (2009) mass functions have been shifted horizontally.

Scaled in this manner, there is an approximate 1-to-1 correlation between the Taurus CMF and IMF above a mass of ~ 0.3 $M_\odot$, but a deficit in the CMF compared to the IMF below this. Although, given an uncertainty of ~ 2 in core masses, assuming standard dust mass opacity uncertainties, a horizontal shift of the same magnitude between the CMF and IMF cannot be ruled out (cf. section 6 of Paper I).

7 SUMMARY AND CONCLUSIONS

In this paper, we have used SPIRE and PACS parallel-mode maps to map and characterize the dense cores and filaments towards the TMC1 region in Taurus. Our principal conclusions can be summarized as follows:

(i) The region mapped by this paper includes approximately 2000 $M_\odot$ of material of which 34 per cent is above an extinction of $A_V \sim 3$ mag. This approximate threshold appears as breaks in the cumulative histogram of column density and the column density PDF, and is the minimum background column density at which prestellar cores are found. Above this value, cores are shown to form more efficiently with increasing background density, reaching a peak around $A_V \sim 14$.

(ii) A total of 35 robust filaments are identified following the methodology described in Arzoumanian et al. (2019). The inner FWHM widths of these filaments are consistent with earlier studies. The supercritical TMC1 filaments are aligned orthogonal to the bulk magnetic field direction. However, there are relatively few of these overall and only $\sim 10\%$ of filaments have peak column densities in excess of an equivalent of $A_v \approx 7-8$.

(iii) The chemical young TMC1 filament is shown to be thermally supercritical. The South filament is largely undifferentiated.

(iv) A catalogue of 44 robust and candidate prestellar cores is tabulated from across the TMC1 region that is 85 per cent complete above a core mass of 0.1 $M_\odot$. The identified prestellar cores have a median temperature of 11.4 K and a median mass of 0.33 $M_\odot$.

(v) Star formation in the TMC1 region appears to be occurring at lower extinctions than other regions, with only 10 per cent of all filaments having an average extinction above 7–8 mag.

(vi) The prestellar CMF for Taurus (L1495 and TMC1 regions combined) is well fit by a single lognormal distribution and is comparable with the standard IMF (e.g. Chabrier 2003). The prestellar CMF, however, does differ from the specific IMF derived for Taurus derived by Luhman et al. (2009).

ACKNOWLEDGEMENTS

SPIRE has been developed by a consortium of institutes led by Cardiff University (UK) and including Univ. Lethbridge (Canada); NAOC (China); CEA, LAM (France); IFSI, Univ. Padua (Italy); IAC (Spain); Stockholm Observatory (Sweden); Imperial College London, RAL, UCL-MSSL, UKATC, Univ. Sussex (UK); and Caltech, JPL, NHSC, Univ. Colorado (USA). This development has been supported by national funding agencies: CSA (Canada); NAOC (China); CEA, CNES, CNRS (France); ASI (Italy); MCINN (Spain); SNSB (Sweden); STFC, UKSA (UK); and NASA (USA).

PACS has been developed by a consortium of institutes led by MPE (Germany) and including UVIE (Austria); KU Leuven, CSL, IMEC (Belgium); CEA, LAM (France); MPIA (Germany); INAF-IFSI/OAA/OAP/OAT, LENS, SISSA (Italy); IAC (Spain). This development has been supported by the funding agencies BMVIT (Austria), ESA-PRODEX (Belgium), CEA/CNES (France), DLR (Germany), ASI/INAF (Italy), and CICYT/MCYT (Spain).

Based on observations obtained with Planck (http://www.esa.int/Planck), an ESA science mission with instruments and contributions directly funded by ESA member states, NASA, and Canada.

The first author thanks J Cernicharo and A Hacar for useful discussions on column density comparisons.

SB and NS acknowledge support by the French ANR and the German DFG through the project 'GENESIS' (ANR-16-CE92-0035-01/DFG1591/2-1).

DATA AVAILABILITY

The data used in this paper, the full catalogue, and other HGBS data products, which include Herschel images and the column density and dust temperature maps are available from the HGBS website at http://gouldbelt-herschel.cea.fr/archives.

REFERENCES

André P. et al., 2010, A&A, 518, L102
André P., Di Francesco J., Ward-Thompson D., Inutsuka S. I., Pudritz R. E., Pineda J. E., 2014, in Beuther H., Klessen R. S., Dullemond C. P., Henning T., eds, Protostars and Planets VI. University of Arizona Press, Tucson, p. 27
André P. J., Palmeirim P., Arzoumanian D., 2022, A&A, 667, L1
Aniano G., Draine B. T., Gordon K. D., Sandstrom K., 2011, PASP, 123, 1218
Arzoumanian D. et al., 2011, A&A, 529, L6
Arzoumanian D. et al., 2019, A&A, 621, A42
Benedettini M. et al., 2018, A&A, 619, A52
Bernard J.-P. et al., 2010, A&A, 518, L88
Bohlin R. C., Savage B. D., Drake J. F., 1978, ApJ, 224, 132
Bonnor W. B., 1956, MNRAS, 116, 351
Bresnahan D. et al., 2018, A&A, 615, A125
Brunt C. M., 2010, A&A, 513, A67
Cernicharo J., Bachiller R., 1984, A&AS, 58, 327
Chabrier G., 2003, PASP, 115, 763
Dharmawardena T. E., Bailer-Jones C. A. L., Fouesneau M., Foreman-Mackey D., 2022, A&A, 658, A166
Di Francesco J. et al., 2020, ApJ, 904, 172
Dobashi K., Shimoikura T., Nakamura F., Kameno S., Mizuno I., Taniguchi K., 2018, ApJ, 864, 82
Ebert R., 1955, ZAp, 37, 217
Elmegreen B. G., Falgarone E., 1996, ApJ, 471, 816
Esplin T. L., Luhman K. L., 2019, AJ, 158, 54
Federrath C., Klessen R. S., 2013, ApJ, 763, 51
Fehér O., Tóth L. V., Ward-Thompson D., Kirk J., Kraus A., Pelkonen V.-M., Pintér S., Zahorecz S., 2016, A&A, 590, A75
Fleming G. D., Kirk J. M., Ward-Thompson D., Pattle K., 2019, preprint (arXiv:1904.06980)
Fuente A. et al., 2019, A&A, 624, A105
Galli P. A. B. et al., 2019, A&A, 630, A137
Gould B., 1879, Uranometria Argentina, Resultados del Observatorio Nacional Argentino en Cordoba Vol. 1. P.E. Coni, Buenos Aires
Griffin M. J. et al., 2010, A&A, 518, L3
Heiles C. E., 1968, ApJ, 151, 919
Helou G., Madore B. F., Schmitz M., Bicay M. D., Wu X., Bennett J., 1991, in Albrecht M. A., Egret D., eds, Astrophysics and Space Science Library, Vol. 171, Databases and On-line Data in Astronomy. Kluwer, London, p. 89
Herschel J., 1847, Results of Astronomical Observations Made at the Cape of Good Hope. Smith, Elder, and Co., London
Hildebrand R. H., 1983, Q. J. R. Astron. Soc., 24, 267
Hill T. et al., 2011, A&A, 533, A94
Inutsuka S.-i., Miyama S. M., 1997, ApJ, 480, 681
Ivanova A., Lallement R., Vergely J. L., Hottier C., 2021, A&A, 652, A22
Juvela M., Montillaud J., 2013, A&A, 557, A73
Juvela M., Malinen J., Lunttila T., 2013, A&A, 553, A113
Kauffmann J., Bertoldi F., Bourke T. L., Evans N. J. II, Lee C. W., 2008, A&A, 487, 993
Kenyon S. J., Dobrzycka D., Hartmann L., 1994, AJ, 108, 1872
Kirk J. M. et al., 2013, MNRAS, 432, 1424
Könyves V. et al., 2015, A&A, 584, A91
Kraus A. L., Herczeg G. J., Rizzuto A. C., Mann A. W., Slesnick C. L., Carpenter J. M., Hillenbrand L. A., Mamajek E. E., 2017, ApJ, 838, 150
Krolikowski D. M., Kraus A. L., Rizzuto A. C., 2021, AJ, 162, 110
Lada C. J., Lombardi M., Alves J. F., 2010, ApJ, 724, 687
Ladjelate B. et al., 2020, A&A, 638, A74
Loinard L., Torres R. M., Mioduszewski A. J., Rodríguez L. F., 2008, Revista Mexicana de Astronomia y Astrofisica Conference Series, Vol. 34. Instituto de Astronomía, Universidad Nacional Autónoma de México, Mexio City, p. 14

Lombardi M., Alves J., Lada C. J., 2015, A&A, 576, L1
Luhman K. L., 2018, AJ, 156, 271
Luhman K. L., Mamajek E. E., Allen P. R., Cruz K. L., 2009, ApJ, 703, 399
Lynds B. T., 1962, ApJS, 7, 1
McGuire B. A., Burkhardt A. M., Kalenskii S., Shingledecker C. N., Remijan A. J., Herbst E., McCarthy M. C., 2018, Science, 359, 202
Markwardt C. B., 2009, in Bohlender D. A., Durand D., Dowler P., eds, ASP Conf. Ser. Vol. 411, Astronomical Data Analysis Software and Systems XVIII. Astron. Soc. Pac., San Francisco, p. 251
Marsh K. A. et al., 2016, MNRAS, 459, 342 (Paper I)
Men'shchikov A., André P., Didelon P., Motte F., Hennemann M., Schneider N., 2012, A&A, 542, A81
Miville-Deschênes M.-A. et al., 2010, A&A, 518, L104
Nakamura F., Kameno S., Kusune T., Mizuno I., Dobashi K., Shimoikura T., Taniguchi K., 2019, PASJ, 71, 117
Nutter D., Kirk J. M., Stamatellos D., Ward-Thompson D., 2008, MNRAS, 384, 755
Ott S., 2010, in Mizumoto Y., Morita K.-I., Ohishi M., eds, ASP Conf. Ser. Vol. 434, Astronomical Data Analysis Software and Systems XIX. Astron. Soc. Pac., San Francisco, p. 139
Palmeirim P. et al., 2013, A&A, 550, A38
Panopoulou G. V., Psaradaki I., Skalidis R., Tassis K., Andrews J. J., 2017, MNRAS, 466, 2529
Pezzuto S. et al., 2021, A&A, 645, A55
Pilbratt G. L. et al., 2010, A&A, 518, L1
Planck Collaboration XI, 2014, A&A, 571, A11
Planck Collaboration XXVIII, 2016, A&A, 594, A28
Planck Collaboration XI, 2020, A&A, 641, A11
Poglitsch A. et al., 2010, A&A, 518, L2
Rebull L. M. et al., 2010, ApJS, 186, 259
Roussel H., 2013, PASP, 125, 1126
Roy A. et al., 2013, ApJ, 763, 55
Roy A. et al., 2014, A&A, 562, A138
Roy A. et al., 2019, A&A, 626, A76
Schisano E. et al., 2020, MNRAS, 492, 5420
Schneider N. et al., 2011, A&A, 529, A1
Schneider N. et al., 2013, ApJ, 766, L17
Schneider N. et al., 2015, A&A, 575, A79
Soma T., Sakai N., Watanabe Y., Yamamoto S., 2018, ApJ, 854, 116
Sousbie T., 2011, MNRAS, 414, 350
Straizys V., Meistas E., 1980, Acta Astron., 30, 541
Swinyard B. M. et al., 2010, A&A, 518, L4
Tóth L. V., Haas M., Lemke D., Mattila K., Onishi T., 2004, A&A, 420, 533
Uehara H., Dobashi K., Nishiura S., Shimoikura T., Naoi T., 2021, ApJ, 915, 74

SUPPORTING INFORMATION

Supplementary data are available at *MNRAS* online.

Table B1. Catalogue of dense cores identified in the HGBS maps of the TMC1 Region of the Taurus molecular cloud.
Table B2. Derived properties of the dense cores identified in the HGBS maps of the TMC1 Region of the Taurus molecular cloud (template).

Please note: Oxford University Press is not responsible for the content or functionality of any supporting materials supplied by the authors. Any queries (other than missing material) should be directed to the corresponding author for the article.

APPENDIX A: INDIVIDUAL WAVELENGTH IMAGES

Figs A1–A5 show the individual *Herschel* flux maps for the TMC1 region. Details are listed in the caption to Fig. A1. The data reduction process is described in Section 2.

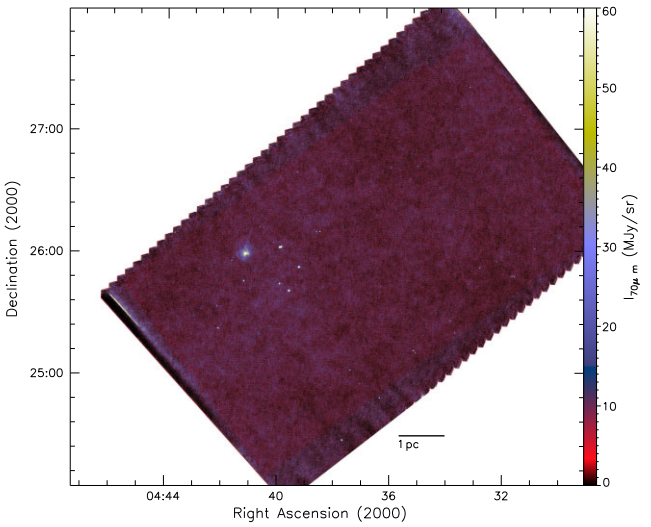

Figure A1. *Herschel* map of submillimetre dust emission at 70 μm towards the TMC1 region, as detected by *Herschel*'s PACS instrument. The maps have been corrected for the IRAS/Planck DC offset (see Section 4). The horizontal scale bar shows 1 pc at the assumed distance to Taurus (140 pc).

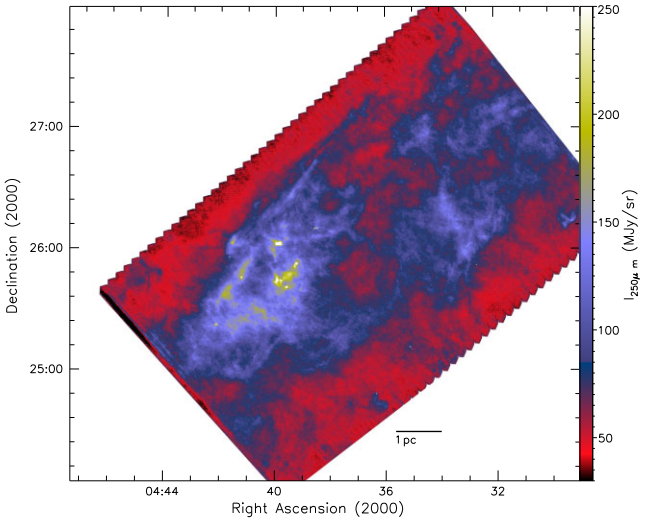

Figure A2. *Herschel* map of submillimetre dust emission at 160 μm towards the TMC1 region, as detected by *Herschel*'s PACS instrument. Details as Fig. A1.

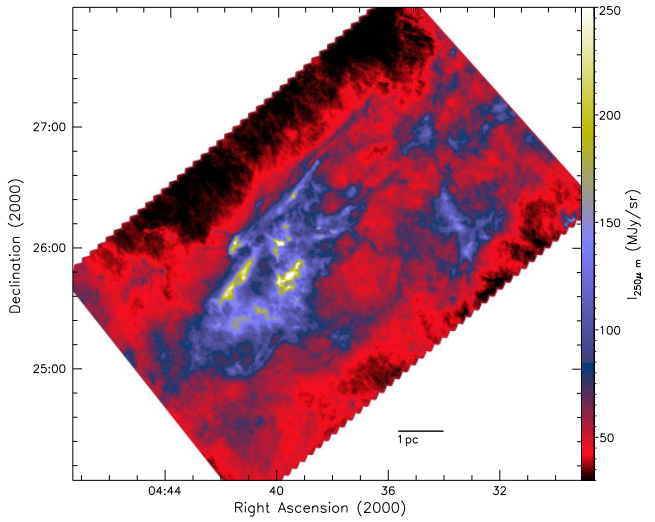

Figure A3. *Herschel* map of submillimetre dust emission at 250 μm towards the TMC1 region, as detected by *Herschel*'s SPIRE instrument. Details as Fig. A1.

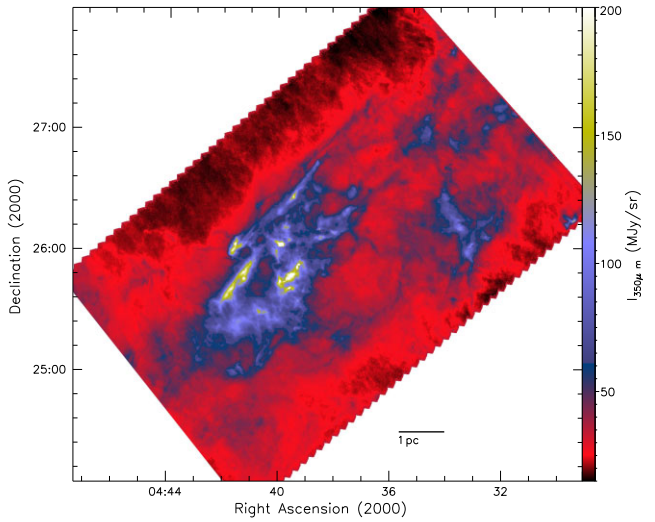

Figure A4. *Herschel* map of submillimetre dust emission at 350 μm towards the TMC1 region, as detected by *Herschel*'s SPIRE instrument. Details as Fig. A1.

APPENDIX B: DENSE CORE CATALOGUE

Table B1 shows the first three lines of the catalogue, the rest being available online. Each column of the table is numbered. Catalogue entries are as follows:

(1) Core number;

(2) Core name = HGBS_J prefix directly followed by a tag created from the J2000 sexagesimal coordinates;

(3) and **(4)**: RA and declination of core centre;

(5), **(15)**, **(25)**, **(35)**, and **(45)**: Detection significance from monochromatic single scales, in the 70-, 160-, 250-, 350-, and 500-μm maps, respectively.

(6)±**(7)**, **(16)**±**(17)**(**26**)±(**27**)(**36**)±(**37**)(**46**)±(**47**): Peak flux density and its error in Jy/beam as estimated by *getsources*;

(8), **(18)**, **(28)**, **(38)**, **(48)**: Contrast over the local background, defined as the ratio of the background-subtracted peak intensity to the local background intensity ($S_{\lambda}^{\rm peak}/S_{\rm bg}$);

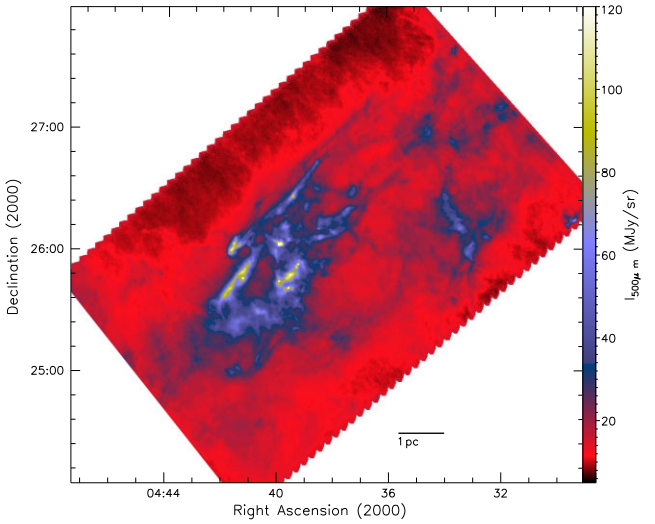

Figure A5. *Herschel* map of submillimetre dust emission at 500 μm towards the TMC1 region, as detected by *Herschel*'s SPIRE instrument. Details as Fig. A1.

(9), **(19)**, **(29)**, **(39)**: Peak flux density measured after smoothing to a 36.3 arcsec beam;

(10)±**(11)**, **(20)**±**(21)**, **(30)**±**(31)**, **(40)**±**(41)**, **(49)**±**(50)**: Integrated flux density and its error in Jy as estimated by *getsources*;

(12)–**(13)**, **(22)**–**(23)**, **(32)**–**(33)**, **(42)**–**(43)**, **(51)**–**(52)**: Major and minor FWHM diameters of the core (in arcsec), respectively, as estimated by *getsources*.

(14), **(24)**, **(34)**, **(44)**, **(53)**: Position angle of the core major axis, measured east of north, in degrees;

(54) Detection significance in the high-resolution column density image;

(55) Peak H_2 column density in units of 10^{21} cm^{-2} as estimated by *getsources* in the high-resolution column density image;

(56) Column density contrast over the local background, as estimated by *getsources* in the high-resolution column density image;

(57) Peak column density measured in a 36.3 arcsec beam;

(58) Local background H_2 column density as estimated by *getsources* in the high-resolution column density image;

(59)–**(60)**–**(61)**: Major and minor FWHM diameters of the core, and position angle of the major axis, respectively, as measured in the high-resolution column density image;

(62) CSAR Counterpart: whether the *getsources* core has a counterpart detected by the *CSAR* source-finding algorithm: 1 and 2 denote when the *CSAR* counterpart is within an ellipse that is respectively equivalent to the half-width or full-width of the *getsources* core as measured on the high-resolution column density map. 3 denotes if the *getsources* core is coincident with extended emission associated with a *CSAR* counterpart.

(63) Number of *Herschel* bands in which the core is significant ($\mathrm{Sig}_{\lambda} > 5$) and has a positive flux density, excluding the column density plane;

(64) Core type: either protostellar, robust prestellar, candidate prestellar, unbound starless, or other;

Table B2 lists the derived properties of the dense cores, only the first three lines of the catalogue are shown, the rest being available online. Each column of the table is numbered. Entries are as follows:

(1) Core running number; **(2)** Core name = HGBS_J prefix directly followed by a tag created from the J2000 sexagesimal coordinates;

(3) and **(4)**: RA and declination of core centre;

Table B1. Catalogue of dense cores identified in the HGBS maps of the TMC1 Region of the TMC (template, full catalogue only provided online).

C.No.	Source name	RA (2000)	Dec. (2000)	Sig_{70}	S_{70}^{peak}		S_{70}^{peak}/S_{bg}	$S_{70}^{conv,500}$	S_{70}^{tot}		a_{70}	b_{70}	PA_{70}
		(h m s)	(°′″)		(Jy beam^{-1})			(Jy beam$^{-1}_{500}$)	(Jy)		(″)	(″)	(°)
(1)	(2)	(3)	(4)	(5)	(6)	(7)	(8)	(9)	(10)	(11)	(12)	(13)	(14)
6	043222.7 + 270051	04:32:22.75	+ 27:00:51.5	1.3	−5.13e-03	4.0e-03	0.72	−1.05e-01	−1.83e-01	1.4e-01	234	93	119
9	043242.9 + 255231	04:32:42.95	+ 25:52:31.2	93.2	1.48e + 00	1.7e-02	227.83	1.75e + 00	2.05e + 00	2.4e-02	8	8	198
14	043307.9 + 255848	04:33:07.99	+ 25:58:48.5	0.0	9.65e-03	6.0e-03	0.88	2.05e-01	4.85e-01	3.0e-01	178	170	52

Sig_{160}	S_{160}^{peak}		S_{160}^{peak}/S_{bg}	$S_{160}^{conv,500}$	S_{160}^{tot}		a_{160}	b_{160}	PA_{160}	Sig_{250}	S_{250}^{peak}		S_{250}^{peak}/S_{bg}
	(Jy beam^{-1})			(Jy beam$^{-1}_{500}$)	(Jy)		(″)	(″)	(°)		(Jy beam^{-1})		
(15)	(16)	(17)	(18)	(19)	(20)	(21)	(22)	(23)	(24)	(25)	(26)	(27)	(28)
0.0	9.89e-02	3.0e-02	0.50	8.26e-01	2.26e + 01	6.9e + 00	226	192	161	8.1	3.75e-01	3.6e-02	2.57
86.5	2.21e + 00	2.6e-02	45.10	2.62e + 00	2.03e + 00	2.4e-02	13	13	117	109.8	1.64e + 00	3.5e-02	34.78
0.0	3.09e-02	2.0e-02	0.10	2.56e-01	8.84e + 00	5.7e + 00	194	178	189	7.9	2.18e-01	3.0e-02	0.36

$S_{250}^{conv,500}$	S_{250}^{tot}		a_{250}	b_{250}	PA_{250}	Sig_{350}	S_{350}^{peak}		S_{350}^{peak}/S_{bg}	$S_{350}^{conv,500}$	S_{350}^{tot}		a_{350}	b_{350}
(Jy beam$^{-1}_{500}$)	(Jy)		(″)	(″)	(°)		(Jy beam^{-1})			(Jy beam$^{-1}_{500}$)	(Jy)		(″)	(″)
(29)	(30)	(31)	(32)	(33)	(34)	(35)	(36)	(37)	(38)	(39)	(40)	(41)	(42)	(43)
1.47e + 00	2.56e + 01	2.4e + 00	135	131	125	9.4	3.80e-01	5.0e-02	2.03	8.29e-01	1.13e + 01	1.5e + 00	126	108
1.71e + 00	1.36e + 00	2.9e-02	18	18	54	68.3	1.31e+00	5.5e-02	16.67	1.41e + 00	1.10e + 00	4.6e-02	24	24
8.33e-01	8.82e + 00	1.2e + 00	125	95	202	11.2	4.76e-01	1.1e-01	0.66	1.03e + 00	1.06e + 01	2.5e + 00	119	92

PA_{350}	Sig_{500}	S_{500}^{peak}		S_{500}^{peak}/S_{bg}	S_{500}^{tot}		a_{500}	b_{500}	PA_{500}	$Sig_{N(H_2)}$	$N_{H_2}^{peak}$	$N_{H_2}^{peak}/N_{bg}$	$N_{H_2}^{conv,500}$
(°)		(Jy beam^{-1})			(Jy)		(″)	(″)	(°)		(10^{21} cm^{-2})		(10^{21} cm^{-2})
(44)	(45)	(46)	(47)	(48)	(49)	(50)	(51)	(52)	(53)	(54)	(55)	(56)	(57)
110	12.3	4.22e-01	4.1e-02	2.44	6.29e + 00	6.1e-01	127	113	119	13.7	1.77e + 00	0.88	1.65e + 00
152	55.1	8.82e-01	3.8e-02	8.06	7.13e-01	3.0e-02	36	36	180	69.3	4.66e + 00	2.34	1.31e + 00
195	17.4	5.11e-01	6.9e-02	0.64	6.30e + 00	8.5e-01	123	109	202	16.9	1.70e + 00	0.40	1.51e + 00

$N_{H_2}^{bg}$	$a_{N(H_2)}$	$b_{N(H_2)}$	$PA_{N(H_2)}$	CSAR	N_{SED}	
(10^{21} cm^{-2})	(″)	(″)	(°)			
(58)	(59)	(60)	(61)	(62)	(63)	(64)
2.00e + 00	133	102	112	1	3	Unbound starless
2.00e + 00	21	18	170	1	5	Protostellar
4.22e + 00	101	81	187	1	3	Robust prestellar

Note. The header's third row contains column references explained in the main text.

Table B2. Derived properties of the dense cores identified in the HGBS maps of the TMC1 Region of the TMC (template, full table only provided online).

C.No.	Source name	RA (2000) (h m s)	Dec. (2000) (°′″)	$R_{\rm core}$ (pc)		$M_{\rm core}$ ($M_\odot$)		$T_{\rm core}$ (K)		$N_{\rm H_2}^{\rm peak}$ (10^{21} cm^{-2})	$N_{\rm H_2}^{\rm ave}$ (10^{21} cm^{-2})	
(1)	(2)	(3)	(4)	(5)	(6)	(7)	(8)	(9)	(10)	(11)	(12)	(13)
6	043222.7 + 270051	04:32:22.75	+ 27:00:51.5	0.079	0.078	0.276	0.081	14.9	1.3	1.80e + 21	6.1e-01	6.3e-01
9	043242.9 + 255231	04:32:42.95	+ 25:52:31.2	0.013	0.005	0.024	0.005	14.4	0.6	1.64e + 21	1.9e + 00	1.3e + 01
14	043307.9 + 255848	04:33:07.99	+ 25:58:48.5	0.062	0.060	1.035	0.416	9.5	0.8	4.93e + 21	3.8e + 00	4.0e + 00

	$n_{\rm H_2}^{\rm ave}$ (10^4 cm^{-3})	$\alpha_{\rm BE}$	Core type	Comments
(14)	(15)	(16)	(17)	(18)
1.9e-01	1.9e-01	8.2	Unbound starless	
3.4e + 00	6.3e + 01	5.9	Protostellar	
1.5e + 00	1.6e + 00	1.1	Robust prestellar	

Note. The header's third row contains column references explained in the main text.

(5) and **(6)**: Geometrical average between the major and minor FWHM sizes of the core (in pc), as measured in the high-resolution column density map before deconvolution, and after deconvolution from the 18.2 arcsec HPBW resolution of the map, respectively. (NB: Both values provide estimates of the object's outer *radius* when the core can be approximately described by a Gaussian distribution, as is the case for a critical Bonnor-Ebert spheroid);

(7) Estimated core mass ($M_\odot$) assuming the dust opacity law advocated by Roy et al. (2014); **(9)** SED dust temperature (K); **(8)** and **(10)** Statistical errors on the mass and temperature, respectively, including calibration uncertainties, but excluding dust opacity uncertainties;

(11) Peak H_2 column density, at the resolution of the 500 μm data, derived from a graybody SED fit to the core peak flux densities measured in a common 36.3 arcsec beam at all wavelengths;

(12) Average column density, calculated as $N_{\rm H_2}^{\rm ave} = \frac{M_{\rm core}}{\pi R_{\rm core}^2} \frac{1}{\mu m_{\rm H}}$, where $M_{\rm core}$ is the estimated core mass (col. **7**), $R_{\rm core}$ the estimated core radius prior to deconvolution (col. **6**), and $\mu = 2.86$;

(13) Average column density calculated in the same way as for col. **12** but using the deconvolved core radius (col. **5**) instead of the core radius measured prior to deconvolution;

(14) Average volume density, calculated as $n_{\rm H_2}^{\rm ave} = \frac{M_{\rm core}}{4/3\pi R_{\rm core}^3} \frac{1}{\mu m_{\rm H}}$, using the estimated core radius prior to deconvolution;

(15) Average volume density, calculated in the same way as for col. **15** but using the deconvolved core radius (col. **5**) instead of the core radius measured prior to deconvolution;

(16) Bonnor-Ebert mass ratio: $\alpha_{\rm BE} = M_{\rm BE,crit}/M_{\rm obs}$ (see text for details);

(17) Core type: either protostellar, robust prestellar, candidate prestellar, unbound starless, or other;

(18) Comments may be *no SED fit*.

This paper has been typeset from a TEX/LATEX file prepared by the author.